JOURNAL OF PETROLOGY | VOLUME 52 | NUMBER 12 | PAGES 2461–2482 | 2011 | doi:10.1093/petrology/egr052

Thermodynamic Model for the Effect of Post-entrapment Crystallization on the H_2O–CO_2 Systematics of Vapor-saturated, Silicate Melt Inclusions

MATTHEW STEELE-MACINNIS, ROSARIO ESPOSITO AND ROBERT J. BODNAR*

FLUIDS RESEARCH LABORATORY, DEPARTMENT OF GEOSCIENCES, VIRGINIA TECH, BLACKSBURG, VA 24061, USA

RECEIVED JULY 8, 2010; ACCEPTED OCTOBER 5, 2011

Melt inclusions (MI) represent the best source of information concerning the pre-eruptive volatile contents of magmas. If the trapped melt is enriched in volatile species, following trapping the MI may generate a vapor bubble containing volatiles that have exsolved from the melt. Thermodynamic modeling of vapor-saturated albitic composition ($NaAlSi_3O_8$) MI shows that the CO_2 content of the melt phase in the MI is sensitive to small amounts of post-entrapment crystallization (PEC), whereas the H_2O content of the melt is less sensitive to PEC. During PEC, CO_2 is transferred from the melt to the vapor phase and the vapor bubble may contain a significant amount, if not most, of the CO_2 in the MI. The contrasting behaviors of H_2O and CO_2 during PEC lead to H_2O–CO_2 trends that are similar to those predicted for open-system degassing during magma ascent and decompression. Thus, similar H_2O–CO_2 trends may be produced if (1) vapor-saturated MI are trapped at various depths along a magmatic ascent path, or (2) MI having the same volatile content are all trapped at the same depth, but undergo different amounts of PEC following trapping. It is not possible to distinguish between these two contrasting interpretations based on MI volatile data alone. However, by examining the volatile trends within the context of other geochemical monitors of crystallization or magma evolution progress, it may be possible to determine whether the volatile trends were generated along a degassing path or if they reflect various amounts of PEC in an originally homogeneous melt inclusion assemblage. The volatile trends resulting from PEC of MI described in this study are directly applicable to silica-rich (granitic) MI trapped in non-ferromagnesian host phases, and are only qualitatively applicable to more mafic melt compositions and/or host phases owing to modifications resulting from Fe exchange with the host and to post-entrapment re-equilibration processes.

KEY WORDS: *melt inclusions; volatiles; post-entrapment crystallization; magmatic degassing; H_2O–CO_2*

INTRODUCTION

Silicate melt inclusions (MI) represent samples of melt that are trapped during growth of igneous phenocrysts in a crystallizing magma body, and today MI are one of the major tools used to study igneous petrogenesis (Roedder, 1979; Lowenstern, 1995, 2003; Sobolev, 1996; Frezzotti, 2001; Danyushevsky *et al.*, 2002; Kent, 2008; Métrich & Wallace, 2008). Once the melt inclusion has become completely enclosed by the host phenocryst and isolated from the surrounding bulk melt from which the phenocryst is continuing to precipitate, the MI may continue to evolve physically and chemically, independent of the evolution of the melt outside of the phenocryst. At the moment that the MI is isolated from the bulk melt, it is unlikely to have a morphology that represents the minimum surface free energy of the system (sphere or negative-crystal shape). As a result, the MI will continue to mature through dissolution of material from the walls and re-precipitation elsewhere on the walls to achieve the lowest energy state, in a manner similar to the evolution

*Corresponding author. Telephone: 1-540-231-7455. E-mail: rjb@vt.edu

in morphology that fluid inclusions undergo after trapping (see Roedder, 1984, fig. 2-15; Bodnar *et al.*, 1989). If dissolution and re-precipitation on the walls occurs in a closed system at essentially constant *PT* conditions, little or no net mass may be transferred from the melt phase into the host and the composition of the MI will not be affected by this morphological maturation process (Manley, 1996). If the host magma is subsequently erupted to the surface and cools rapidly (preventing significant crystallization on the walls of the MI), the MI may be preserved as a homogeneous, single-phase glass (Fig. 1). In such cases, the MI are usually studied 'as found', and the assumption that the glass composition represents the composition of melt in equilibrium with the host phase at the time of trapping is probably valid.

If, following trapping, the phenocryst containing the MI cools relatively slowly, the MI may be modified in one of several ways. In the simplest case, some material from the melt may crystallize on the inclusion walls during cooling, resulting in a single-phase, homogeneous glass MI that has had some material removed and precipitated as host crystal. This post-entrapment crystallization (PEC) can occur while the phenocryst still resides in the magma chamber, or during ascent to the surface, or at the Earth's surface, perhaps at the bottom of a volcanic pile or the base of a lava flow (where cooling rates are slower compared with the lava–air interface). If PEC occurs in any of these environments, the composition of the remaining melt (glass) phase in the MI may be significantly modified. Danyushevsky (2001) has developed an approach to account for PEC-induced changes in composition for MI in olivine.

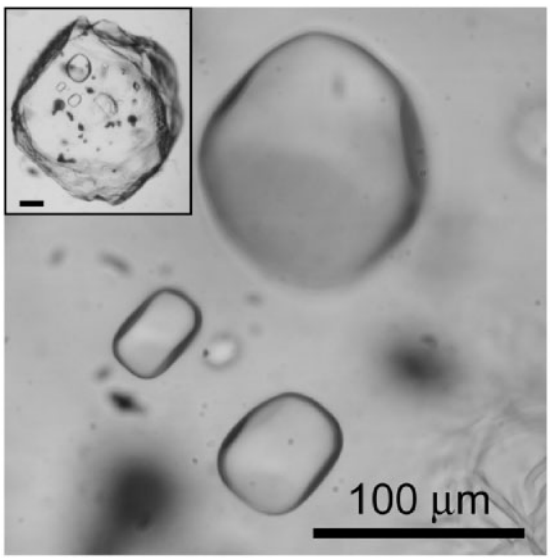

Fig. 1. Quartz phenocryst from the Bishop Tuff (inset) showing three large, glassy melt inclusions, with the two smaller inclusions in the lower left–center exposed on the crystal surface.

Larger MI and those that cooled somewhat more slowly often contain multiple phases when observed at room temperature, and may consist of any combination of glass, daughter crystals that grew from the melt during cooling, and one or more vapor bubbles (Roedder, 1984). Ideally, one would heat these MI in the laboratory to return the inclusion contents to a single, homogeneous melt state and then quench the MI to a glass before conducting microanalysis to determine the composition (Fig. 2; top). However, heating MI to homogenization can be problematic in some cases. First, many MI decrepitate during heating at 1 atm, owing to the large internal pressures that are generated in volatile-rich MI (Student & Bodnar, 1996; Fedele *et al.*, 2003). In some cases, decrepitation of volatile-rich MI during heating may be eliminated or minimized by heating the MI in a hydrothermal vessel under a high confining pressure (Skirius *et al.*, 1990; Webster & Duffield, 1991; Anderson *et al.*, 2000; Thomas *et al.*, 2002; Student & Bodnar, 2004; Bodnar & Student, 2006). Other workers have attempted to reconstruct the bulk composition without the necessity to homogenize the MI by determining the compositions of the various phases contained in the MI and then using their volumetric proportions to estimate the original melt composition (Szabo *et al.*, 1996), and Anderson (2010) recently described a technique involving focused ion beam (FIB) milling and SEM analysis to identify daughter phases and determine the compositions of crystal-rich MI.

A second problem associated with heating MI to return them to their original melt (glass) state is the possibility of diffusive re-equilibration of the inclusion during laboratory heating (Lu *et al.*, 1995; Zajacz *et al.*, 2009). Danyushevsky *et al.* (2000) have documented this behavior for MI in olivine, and Severs *et al.* (2007) have experimentally investigated H_2O loss from MI in quartz during laboratory heating. Gaetani *et al.* (2011) described the effect of post-entrapment diffusion on the H_2O–CO_2 systematics of glassy MI in olivine.

Owing to the problems associated with heating MI to homogenization described above, some workers choose to study the inclusions 'as found'. Depending on the nature of the MI, the host phase, the analytical techniques used, and the problem being studied, this approach may not introduce serious errors. For example, single-phase, glassy MI in quartz, such as those that are common in the Bishop Tuff (Anderson *et al.*, 2000) (Fig. 1), have probably experienced only some small amount of PEC of quartz on the inclusion walls. Thus, whereas the silica content of the melt may be reduced by a few per cent at most if the MI are not heated before analysis, ratios of all other elements in the melt should be relatively unaffected. Additionally, if the study does not involve determination of the pre-eruptive volatile (especially H_2O and/or CO_2) content of the melt, the presence of a vapor bubble is unlikely to

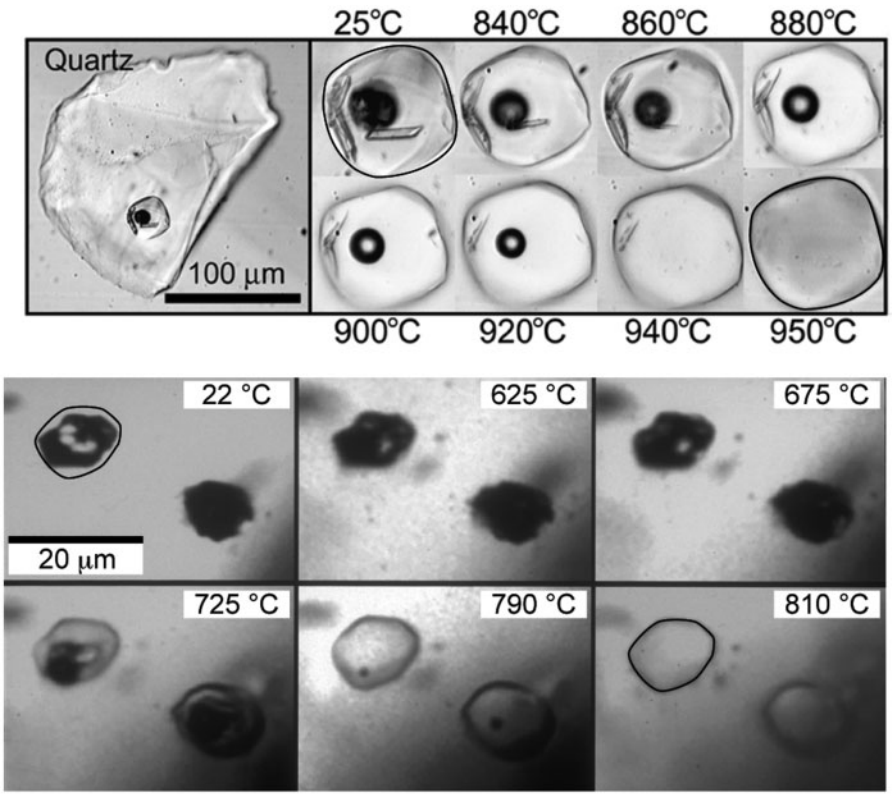

Fig. 2. (Top) Heating sequence for a multi-phase silicate melt inclusion in quartz from the Toba Tuff, Sumatra, showing the melting of various daughter minerals and dissolution of the vapor phase to produce a homogeneous melt (glass). The boundary between the melt and host quartz has been highlighted by a continuous black line in the image taken at 950°C, and this same line has been copied onto the image taken at 25°C to show the amount of quartz host dissolved during heating from 25° to 950°C. It should be noted that little of the quartz host was dissolved during heating. (Bottom) Heating sequence on two completely crystallized MI in a quartz phenocryst from Red Mountain, Arizona, showing the homogenization behavior. The boundary between the melt and host quartz has been outlined by a continuous black line in the MI on the left in the image taken at 810°C, and this is interpreted to represent the size (volume) of the original MI at trapping. The same outline (representing the size of the original trapped MI) has been copied onto the image taken at 22°C to show the amount of quartz host dissolved during heating from 22° to 810°C. The lighter area between the outline and the dark, crystallized MI represents quartz that precipitated on the walls following entrapment. It should be noted that this quartz host on the walls dissolved into the melt during heating from 22° to 810°C (modified from Student & Bodnar, 2004).

significantly affect abundances of major and trace elements in the glass (melt) phase. Finally, if the MI are analyzed by laser ablation inductively coupled plasma mass spectrometry (LA-ICP-MS) to determine only the major and trace element (non-volatile) content of the melt, homogenization of the MI is not necessary because all phases in the MI are sampled quantitatively during the analysis and the analytical results are easily corrected for contributions from the host phase (Halter *et al.*, 2002).

A potentially more serious problem occurs when the MI contains a vapor bubble and the goal of the study is to determine the pre-eruptive volatile content of the melt. The presence of a vapor bubble is especially problematic if the MI trapped a vapor-saturated melt, or if the melt became vapor-saturated as a result of post-entrapment crystallization. In this study, we investigate the effect of post-entrapment crystallization and vapor bubble growth on the volatile content of the melt (glass) in MI. This quantitative model is based on rigorous thermodynamic and experimental data for volatile solubilities in melts and the volumetric properties of the MI system. We emphasize that the model assumes that equilibrium between the melt and volatile and host phases is maintained during cooling, but we also recognize that equilibrium is not always maintained in MI following trapping. We also document that at least in some cases the vapor bubble in MI contains sufficient CO_2 to be detectable by Raman spectroscopy, supporting the interpretation that the vapor bubble may contain a significant portion of the total volatiles in the MI. Finally, we document that H_2O–CO_2 trends that are often interpreted to represent trapping of vapor-saturated melt at various depths during continuous degassing and trapping of MI in an ascending magma can also be produced if a group of MI all trap a melt with the same composition (H_2O and CO_2 content) but undergo varying degrees of post-entrapment crystallization

on the walls, such as might occur if the host phenocrysts are collected from different locations within a volcanic unit.

PREVIOUS STUDIES

Various workers have previously considered the effect of PEC and/or the presence of vapor bubbles on the measured volatile content of the glass phase in MI. Kress & Ghiorso (2004) considered the effect of PEC on the compositions of MI based on thermodynamic modeling using the MELTS software. In the examples presented by those workers, the MI did not contain a vapor bubble and the MI did not become saturated in volatiles as a result of PEC. Based on their model, Kress & Ghiorso (2004) estimated that olivine-hosted MI from the 30 June 1997 Popocatépetl andesite pumice experienced 7·3% PEC that resulted in an increase in the H_2O content from the original 1·3 wt % to the measured 1·4 wt % following PEC. Similarly, orthopyroxene-hosted MI from a more siliceous portion of this same eruption experienced 3% PEC that raised the H_2O content from 2·7 wt % to 2·8 wt %. Finally, Kress & Ghiorso (2004) reported that an MI in plagioclase from Satsuma–Iwojima, Japan, underwent 29% PEC that increased the H_2O content from the original 2·88 wt % to the measured 3·99 wt % following PEC. Although this amount of PEC is significant, similar amounts of PEC are common in MI from deeper volcanic or plutonic environments (Student & Bodnar, 1996; Bodnar & Student, 2006) (Fig. 2, bottom).

The MI considered by Kress & Ghiorso (2004) did not contain vapor bubbles, but many natural MI do contain one or more vapor bubbles, which are often referred to as 'shrinkage' bubbles. Vapor bubbles in MI may form in various ways, depending on the melt composition and crystallization processes that occur inside the MI after trapping. It is generally accepted that a shrinkage bubble should form as a natural consequence of cooling after MI entrapment, because thermal contraction (shrinkage) of the melt phase is significantly greater than that of the host phenocryst (Roedder, 1979; Lowenstern, 1995, 2003; Schiano, 2003; Métrich & Wallace, 2008). If the trapped MI is volatile-free, then the bubble is essentially a vacuum, as the vapor pressures of dry silicate melts are low.

In contrast, if the entrapped melt contains volatiles, the vapor bubble may contain some of the volatiles that were originally dissolved in the melt phase, as has been recognized by previous workers (see Roedder, 1979; Anderson & Brown, 1993; Cervantes *et al.*, 2002). Skirius *et al.* (1990) noted that CO_2 and H_2O originally dissolved in the melt may be redistributed into vapor bubbles (and hydrous minerals) that form during cooling, and Anderson & Brown (1993) noted a wide range in CO_2 contents of MI in olivine from the 1959 Kilauea Iki eruption and attributed the variation to the transfer of CO_2 from the melt to the vapor bubbles that were found in some MI. Similarly, Cervantes *et al.* (2002) noted that MI in olivine from Puu Wahi at Mauna Loa, Hawaii, all contained vapor bubbles and showed CO_2 contents ranging from 60 to 180 ppm. When MI from this same sample were heated in the laboratory to homogenize the vapor back into the melt, followed by quenching, the glass contained 300–600 ppm CO_2. Cervantes *et al.* related the difference in CO_2 contents of naturally quenched versus laboratory homogenized MI to the loss of CO_2 to the vapor bubble during cooling in nature.

In some MI, the vapor bubble may contain a relatively dense fluid phase at room temperature. For example, Raman analysis of a vapor bubble in an olivine-hosted MI from the Solchiaro volcano, Procida, Italy, shows peaks characteristic of CO_2 (Fig. 3). The distance between the two peaks of the Fermi diad (Fig. 3) indicates that the density of the fluid in the bubble is $\sim 0{\cdot}17\ g\ cm^{-3}$ [using the equation of Kawakami *et al.* (2003), as modified by Fall *et al.* (2011)]. Assuming that the fluid is pure CO_2, the internal pressure in the bubble is estimated to be 50 bars. Mass-balance calculations indicate that the CO_2 contained in the vapor bubble represents about two-thirds of the total CO_2 in the MI (Table 1).

An important implication of the presence of vapor bubbles in volatile-bearing MI is related to pressures of trapping that are inferred from measured volatile contents of the glass phase, as has been emphasized by Anderson & Brown (1993) and Cervantes *et al.* (2002). Table 2 lists some recent studies in which pressures of formation have been estimated based on data from MI that contain vapor bubbles and/or have experienced various degrees of PEC. Most of the MI are hosted in olivine.

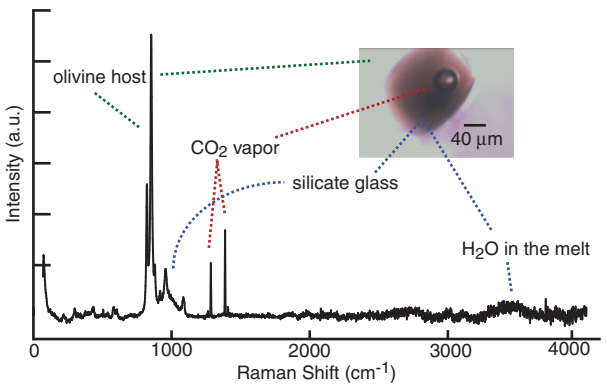

Fig. 3. Raman spectrum of a shrinkage (vapor) bubble in an MI hosted in olivine (inset) from the Solchiaro volcano, Procida, southern Italy. Peaks labeled 'CO_2 vapor' correspond to the Fermi diad for CO_2, and the distance between these peaks varies as a function of the density of the CO_2 phase (Kawakami *et al.*, 2003). Also shown on the spectrum are peaks corresponding to the host (Fo-rich olivine), the silicate glass, and H_2O dissolved in the glass (melt).

Table 1: Calculation of total CO_2 contained in a bubble-bearing MI from Solchiaro (southern Italy)

Parameter	Measured value
Raman spectrum	
Peak 1 (cm^{-1})	1284·33
Peak 2 (cm^{-1})	1387·21
Δ (cm^{-1})	102·88
Vapor bubble	
Vapor density (g cm^{-3})*	$1{\cdot}67 \times 10^{-1}$
Bubble diameter (cm)	$4{\cdot}00 \times 10^{-3}$
Vapor volume (cm^3)†	$3{\cdot}35 \times 10^{-8}$
CO_2 mass (g)	$5{\cdot}60 \times 10^{-9}$
Melt or glass	
Inclusion diameter (cm)	$1{\cdot}50 \times 10^{-2}$
Inclusion volume (cm^3)†	$1{\cdot}77 \times 10^{-6}$
Melt or glass volume (cm^3)‡	$1{\cdot}73 \times 10^{-6}$
Melt or glass density (g cm^{-3})	2·75
Melt or glass mass (g)	$4{\cdot}77 \times 10^{-6}$
Inclusion mass (g)§	$4{\cdot}77 \times 10^{-6}$
Bubble vol. %	1·90%
CO_2 contents	
CO_2 melt (ppm)¶	650
CO_2 in the MI (melt + vapor) (ppm)	1822

CO_2 content of the glass phase was determined using secondary ionization mass spectrometry (SIMS). The CO_2 density in the vapor bubble was determined by Raman spectroscopy. It should be noted that the CO_2 concentration dissolved in the melt (glass) is only 36% of the total CO_2 in the MI, and the bubble accounts for 64% of the total CO_2 in the MI.
*Estimated using the equation of Kawakami *et al.* (2003).
†Volumes estimated from the MI or bubble diameters assuming spherical geometry.
‡Melt or glass volume = inclusion volume − vapor volume.
§Inclusion mass = melt or glass mass + vapor mass.
¶Measured using SIMS.

Because olivine–silicate melt equilibrium is well characterized, it is possible to accurately estimate the percentage of PEC that has occurred in olivine-hosted MI (Danyushevsky, 2001). The volume per cent of the MI occupied by the bubble for studies listed in Table 2 ranged up to 20% (Spilliaert *et al.*, 2006), although most of the bubble-bearing MI showed <10% PEC. All of the studies listed in Table 2 reported a wide range of CO_2 concentrations in the glass, and thus a wide range in the estimated pressures of entrapment. This wide range in CO_2 contents and calculated trapping pressures for MI containing vapor bubbles and that have experienced PEC is consistent with results of the present study described below.

CONCEPTUAL MODEL

Our conceptual model for the *PVTX* evolution in volatile-bearing MI during post-entrapment crystallization is constrained by Roedder's Rules as applied to MI by Bodnar & Student (2006), and assuming chemical equilibrium is maintained at each step. Therefore, in our conceptual model:

(1) the MI is entrapped as a homogeneous, single-phase silicate melt;
(2) the total mass and bulk composition of the MI, represented by melt + vapor + crystal formed during PEC, do not change after entrapment;
(3) the system is isochoric and the total volume of the MI, represented by melt + vapor + crystal formed during PEC, is constant after entrapment;
(4) phase changes (crystallization, vapor exsolution) occur at the equilibrium phase boundaries.

Conditions (1)–(3) represent Roedder's Rules, whereas condition (4) assumes chemical equilibrium. In addition to these four constraints, we specify

(5) the melt phase is saturated in volatiles (H_2O, CO_2 or H_2O–CO_2) at the time of entrapment.

Condition (5) is added because any interpretation of volatile contents in natural MI in the context of magmatic degassing ('degassing paths') requires that MI trap a vapor-saturated melt. It follows from condition (5) that the MI is trapped at *PTX* conditions that are on the vapor-saturated solidus (Fig. 4), as discussed in detail below. Our model may be easily modified to accommodate trapping of a melt that is originally volatile-undersaturated, but that later becomes saturated as a result of PEC (see Student & Bodnar, 1996, fig. 4E and F).

We acknowledge that some or all of conditions (1)–(5) may be violated in some natural MI. However, the assumed conditions represent a reasonable approximation for many natural MI. Bodnar & Student (2006) described the petrographic procedures necessary to identify melt inclusion assemblages (MIA), combined with microthermometry and microanalysis to demonstrate that MI adhere to Roedder's Rules [conditions (1)–(3)]. The isochoric condition [condition (3)] is a reasonable approximation for MI because the compressibility and thermal expansion of the host phase are small in comparison with the melt (± vapor). In our model, as in that of Student & Bodnar (1996), the volume of the MI includes the volume of host phase precipitated on the inclusion walls during PEC. The equilibrium condition [condition (4)] is certainly violated in many natural MI because they contain a silicate glass, which is a metastable phase. However, evidence of nucleation and growth of crystals and bubbles in natural MI is commonly observed, and can be approximated by equilibrium behavior down to the glass transition temperature

Table 2: Studies that report relationships between PEC, presence or absence of shrinkage (vapor) bubbles, and dissolved volatile contents and pressure estimates from natural MI

Reference	Locality	MI host	MI petrography	V_b/V_{MI}	PEC	CO_2 in glass (ppm)	CO_2 in bubble	Pressure (kbar)	Notes
Spilliaert *et al.* (2006)	Etna (Italy)	ol	40–200 μm, bubble-bearing	4–8%, (few 10–20%)	<6%	150–3145	Detected*	0·25–4·25†	MI in same crystal have >1000 ppm range in CO_2
Collins *et al.* (2009)	Etna (Italy)	ol	>35 μm	n.r.	<10%	60–4000	n.r.	0–3·20†	
Hauri (2002)	Hawaii	ol	Some bubble-bearing	n.r.	<12%	5–862	n.r.		CO_2 varies widely for MI within same crystal
Mangiacapra *et al.* (2008)	Campi Flegrei (Italy)	ol, cpx	Glassy, some bubble-bearing	n.r.	n.r.	200–1200	n.r.	0·50–2·0‡	Volitile-poor MI are not included in this study
Vigouroux *et al.* (2008)	Trans-Mexican volcanic belt	ol	Detailed (see their table 2)	wide range (see their table 2)	<16%	b.d.l.–5300	Indicated	≤7·5†	Bubbles may be trapped along with melt
Walker *et al.* (2003)	SE Guatemala	ol	Most 45–85 μm, all bubble-bearing	n.r.	<7%	Mostly 300–2000	n.r.	0·50–5·0†	
Johnson *et al.* (2008)	Central Mexico	ol	Fully enclosed, glassy, some bubble-bearing	n.r.	<20·6	b.d.l.–2500 (1 site ≤6000)	Indicated	≤3·0†	
Anderson & Brown (1993)	Kilauea Iki (Hawaii)	ol	2 types: bubble-free and bubble-bearing	16 MI 2·1–3·0%, 6 MI 4·1–7·0%	n.r.	b.d.l. (<400) (1 MI ~800)	Calculated§	41 MI < 1, 9 > 1†	MI within same aggregates show wide range in CO_2
Cervantes & Wallace (2003)	Xitle (Mexico)	ol	2 types: bubble-free and bubble-bearing	<6·2%	<13%	b.d.l. (2 MI 312–338)	n.r.	<8†	
Kamenetsky *et al.* (2007)	Etna (Italy)	ol	Negative crystal shaped, bubble-bearing		n.r.		Indicated		Ca–Mg carbonates detected in bubble using Raman
Sisson & Layne (1993)	Various back-arc	ol	Spherical to elliptical, 5–150 μm	<1–20%	0–11%	n.r.	n.r.	n.r.	
Saito *et al.* (2001)	Satsuma-Iwojima	plg, cpx opx	Assumed spherical	0·1–9%	n.r.	b.d.l.–300	n.r.	0·20–<1·50†	

ol, olivine; opx, orthopyroxene; plg, plagioclase; cpx, clinopyroxene; opx, orthopyroxene. n.r., not reported; b.d.l., below detection limit.
*CO_2 detected using nuclear microprobe.
†Calculated from H_2O–CO_2 contents using the model of Newman & Lowenstern (2002).
‡Calculated from H_2O–CO_2 contents using the model of Papale *et al.* (2006).
§Calculated from the CO_2 vapor pressure determined from the glass analysis, at 1200°C.

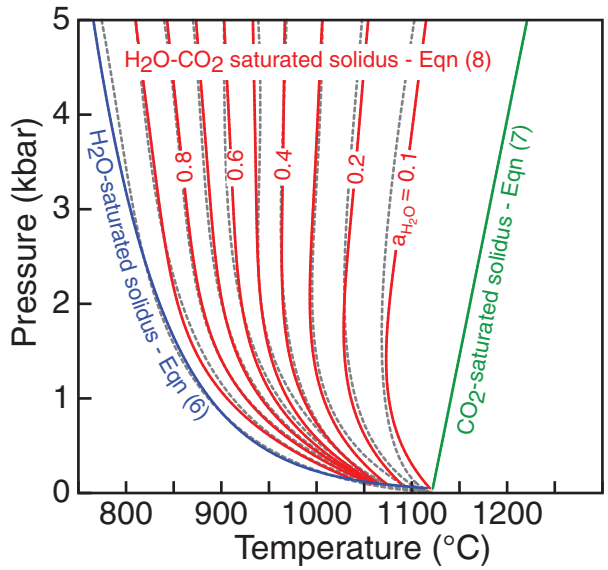

Fig. 4. *PTX* vapor-saturated phase relations in the $NaAlSi_3O_8$–H_2O, $NaAlSi_3O_8$–CO_2 and $NaAlSi_3O_8$–H_2O–CO_2 systems. The *PT* coordinates for the $NaAlSi_3O_8$–H_2O vapor-saturated solidus were calculated using equation (6), the *PT* coordinates for the $NaAlSi_3O_8$–CO_2 vapor-saturated solidus were calculated using equation (7), and the *PT* coordinates for the $NaAlSi_3O_8$–H_2O–CO_2 vapor-saturated solidus were calculated using equation (8). Sections through the vapor-saturated solidus for the ternary system are labeled in $a^{melt}_{H_2O}$. The grey dashed curves represent the vapor-saturated solidus as a function of $a^{melt}_{H_2O}$ from Burnham & Davis (1974).

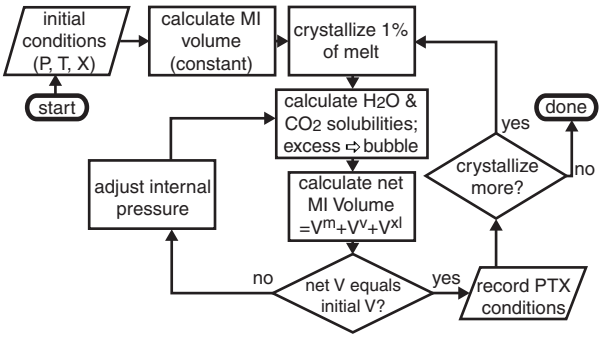

Fig. 5. Schematic flow chart outlining the steps involved in the iterative numerical model used to estimate the *PTX* evolution of volatile-bearing melt inclusions during post-entrapment crystallization.

(which can occur after significant post-entrapment crystallization and bubble growth have occurred).

Within the framework of conditions (1)–(5), we investigate the effects of post-entrapment crystallization on the internal pressure in the inclusion and the volatile composition of the melt phase. Starting with trapping of a single-phase, vapor-saturated melt of known mass, composition and volume, we model the effect of crystallization on the *PVTX* evolution of the MI.

A flow chart outlining the calculation procedure used in the numerical model is shown in Fig. 5. Initial conditions are represented by a fixed mass of melt of known composition trapped as an MI at a known temperature and pressure. Using available *PVTX* data for volatile-bearing melts, the volume of the MI is calculated, then the silicate melt component is allowed to crystallize in 1% increments. The solubilities of H_2O and CO_2 in the melt at the given *P* and *T* are used to calculate the amounts of these volatiles that may be dissolved in the melt—any difference between these values and the total amount in the original melt is assumed to be contained in the vapor bubble. The total volume of the MI after each increment of crystallization, represented by the sum of the volume of remaining melt plus the volume of material that crystallized from the melt plus the volume of the vapor bubble, represents the new volume of the MI. If this new volume equals the original volume, this step in the model is completed and the calculations can be stopped or another increment of crystallization may be examined.

In general, after each stage of crystallization the new volume will not equal the original volume because the sum of the volumes occupied by the crystallized phase and the vapor bubble are not equal to their partial molar volumes in the melt. As a result, because of the requirement of constant volume, the pressure in the inclusion must be adjusted to find a new pressure at which the density of the volatile phase (and, therefore, its volume) and the solubility of the volatile phase in the melt are such that the sum of the volumes (crystals + vapor-saturated melt + vapor bubble) equals the original MI volume. Thus, the model incrementally increases or decreases the pressure, depending on whether the new volume is greater than or less than the original volume, until a pressure is obtained that satisfies the requirement of constant volume and mass of the MI.

Let us consider a melt inclusion with a composition represented by the system $NaAlSi_3O_8$–H_2O–CO_2. Crystallization of some portion of the vapor-saturated melt may be described by the relationship

$$\text{Vapor} - \text{saturated Melt} \rightarrow \text{albite} + \text{vapor} \qquad (1)$$

and the volume change (ΔV_r) of reaction (1) can be expressed as

$$\Delta V_r = X_{NaAlSi_3O_8}\Delta V^{melt\rightarrow xl}_{NaAlSi_3O_8} + X_{H_2O}\Delta V^{melt\rightarrow vapor}_{H_2O} + X_{CO_2}\Delta V^{melt\rightarrow vapor}_{CO_2} \qquad (2)$$

where X_i represents the mole fraction of component *i*, and $\Delta V_i^{\alpha\rightarrow\beta}$ represents the change in volume of component *i* as it moves from phase α to phase β. The volume terms in equation (2) are further given by

$$\Delta V^{melt\rightarrow xl}_{NaAlSi_3O_8} = V^{o,xl}_{NaAlSi_3O_8} - \bar{V}^{melt}_{NaAlSi_3O_8} \qquad (3)$$

$$\Delta V_{H_2O}^{melt\rightarrow vapor} = \bar{V}_{H_2O}^{vapor} - \bar{V}_{H_2O}^{melt} \quad (4)$$

$$\Delta V_{CO_2}^{melt\rightarrow vapor} = \bar{V}_{CO_2}^{vapor} - \bar{V}_{CO_2}^{melt} \quad (5)$$

where $\bar{V}_i^{\alpha}$ is partial molar volume of component i in phase α, and $V_{NaAlSi_3O_8}^{o,xl}$ is the molar volume of crystalline albite at the P and T of the MI. The net ΔV_r of crystallization of a mole of vapor-saturated melt of a given composition is thus a function of the partial molar volumes of $NaAlSi_3O_8$, H_2O and CO_2 in the melt, the partial molar volumes of H_2O and CO_2 in the vapor, and the molar volume of albite. For models involving only a pure (one-component) vapor phase, the partial molar volumes of H_2O and CO_2 in the vapor phase are equal to the molar volumes, and these were calculated using the algorithms of Haar *et al.* (1984) and Holloway (1977, 1987), respectively.

Each of the parameters contributing to the net ΔV_r in equations (2)–(5) vary as functions of P and T, and the partial molar volumes of H_2O and CO_2 in the vapor also vary as functions of the vapor composition (Sterner & Bodnar, 1991). The molar volume of albite ($V_{NaAlSi_3O_8}^{o,xl}$) at the PT conditions considered here is approximately $102 \pm 1\,cm^3\,mol^{-1}$, whereas $\bar{V}_{NaAlSi_3O_8}^{melt}$ is usually $\sim 10\,cm^3\,mol^{-1}$ greater than the molar volume of albite at the same P and T (Burnham & Davis, 1974), yielding a $\Delta V_{NaAlSi_3O_8}^{melt\rightarrow xl}$ of about $10\,cm^3\,mol^{-1}$. In other words, the volume occupied by the crystalline albite is smaller than the volume occupied by albite melt at the same P and T conditions. The partial molar volume of H_2O in the vapor phase, $\bar{V}_{H_2O}^{vapor}$, varies over the range of about $50–150\,cm^3\,mol^{-1}$ (Holloway, 1977, 1987), whereas the partial molar volume of H_2O in the melt, $\bar{V}_{H_2O}^{melt}$, varies between ~ 14 and $22\,cm^3\,mol^{-1}$ (Burnham & Davis, 1971; Lange, 1994), such that $\Delta V_{H_2O}^{melt\rightarrow vapor}$ varies from about $+36$ to $+128\,cm^3\,mol^{-1}$. It should be noted that the large difference between the partial molar volume of H_2O in the melt and the molar volume of H_2O vapor at the same temperature and pressure is the main driver for the large pressure increase associated with exsolution of H_2O from a hydrous melt (Burnham, 1979, 1997; Student & Bodnar, 1996). The partial molar volume of CO_2 in the vapor, $\bar{V}_{CO_2}^{vapor}$, varies over the range $25–115\,cm^3\,mol^{-1}$ (Holloway, 1977, 1987), whereas the partial molar volume of CO_2 in the melt, $\bar{V}_{CO_2}^{melt}$, is about $28{\cdot}6\,cm^3\,mol^{-1}$ (Stolper *et al.*, 1987; Lange, 1994). Thus, $\Delta V_{CO_2}^{melt\rightarrow vapor}$ varies between -3 and $+86\,cm^3\,mol^{-1}$. Given the ranges in values presented above, the volume change associated with vapor-saturated crystallization can thus be negative or positive, depending on the PT conditions and the proportions of $NaAlSi_3O_8$, H_2O and CO_2 in the melt. Because the system is isochoric, the direction of volume change associated with volatile exsolution from the melt thus determines whether the pressure in the MI increases or decreases during PEC and this, in turn, determines whether the volatile content of the remaining melt (glass) in the MI increases or decreases during PEC.

In the isochoric MI model, the net volume change is always zero and we invoke the principle that pressure and volume are inversely related. If PEC predicts an increase in volume (positive ΔV_r), which is not permitted in our constant volume model, then the internal pressure in the MI is increased incrementally to determine the pressure that results in a constant volume. Thus, for an $NaAlSi_3O_8$–H_2O MI, the $NaAlSi_3O_8$ crystallization term [$\Delta V_{NaAlSi_3O_8}^{melt\rightarrow xl}$; equation (3)] predicts a decrease in pressure because the volume change is negative, whereas the H_2O term [$\Delta V_{H_2O}^{melt\rightarrow vapor}$; equation (4)] predicts an increase in pressure during PEC because the volume change is positive. A consequence of the relatively high solubility of H_2O in silicate melt is that the pressure evolution of an H_2O-rich MI during post-entrapment crystallization is controlled by the difference between the partial molar volume of the H_2O component in the melt and the molar volume of H_2O in the vapor, which results in an increase in internal pressure during post-entrapment crystallization (Student & Bodnar, 1996). In contrast, because of the relatively low solubility of CO_2 in silicate melts, the $PVTX$ evolution of a CO_2-rich MI is dominated by the difference between the partial molar volume of the $NaAlSi_3O_8$ component in the melt and the molar volume of crystalline albite, resulting in a decrease in internal pressure during PEC.

The solubilities of H_2O and CO_2 both increase with increasing pressure (Burnham & Davis, 1971; Mysen *et al.*, 1976; Eggler & Kadik, 1979; Hamilton & Oxtoby, 1986; Stolper *et al.*, 1987; Blank *et al.*, 1993). Thus, for an H_2O-rich MI, the internal pressure increases as H_2O exsolves from the melt during crystallization. The increase in pressure increases H_2O solubility in the melt, and H_2O continues to exsolve until a pressure is achieved that satisfies mass and volume balance in the isochoric system (Student & Bodnar, 1996). The net result is that the mass and volume of the H_2O vapor bubble are less than would be expected under isobaric conditions. For the CO_2-rich MI, the decrease in internal pressure caused by post-entrapment crystallization results in decreased CO_2 solubility, and the CO_2 concentration of the melt decreases during PEC. The mass and volume of exsolved CO_2 in the isochoric model are thus greater than they would be if crystallization occurred isobarically.

The evolution of internal pressure in the MI must be accompanied by a systematically related evolution in temperature. The correlation between P and T must be consistent with the Gibbs' Phase Rule and with known phase equilibria in the melt–volatile system (Fig. 4). Because the system under consideration consists of melt plus crystals

plus vapor, *PT* conditions during PEC are constrained to lie on the vapor-saturated solidus. Therefore, as the internal pressure changes in response to crystallization and volatile exsolution, the temperature must change accordingly to remain on the vapor-saturated solidus. Furthermore, for an H_2O-saturated MI, temperature decrease is accompanied by an increase in pressure, whereas for a CO_2-saturated MI, decrease in temperature is accompanied by a decrease in pressure. This behavior is consistent with the above discussion contrasting the evolution of internal *P* during post-entrapment crystallization in H_2O-rich vs CO_2-rich MI. We note that the direction of pressure change during PEC is controlled by the relative change in solubility combined with the difference between the partial molar volumes of the volatiles in the melt compared with their molar volumes, within the constraint that the entire system remains isochoric. The method followed in our numerical model is to incrementally crystallize aliquots of the melt and monitor the bubble growth and evolution of *P* and *T* based on known phase equilibrium and thermodynamic properties of the melt–volatile system. This is accomplished by iterating in pressure to find the *PT* conditions that satisfy mass balance under the restriction that the system must remain isochoric.

DESCRIPTION OF THE QUANTITATIVE THERMODYNAMIC MODEL

Numerical representation of the $NaAlSi_3O_8$–H_2O–CO_2 system

To investigate quantitatively the *PVTX* evolution in an MI during post-entrapment crystallization, numerical formulations are required to represent the phase equilibria, volatile solubilities and volumetric properties of all phases. In this study, we apply a system of theoretical and empirical thermodynamic expressions to model the systems $NaAlSi_3O_8$–H_2O, $NaAlSi_3O_8$–CO_2, and $NaAlSi_3O_8$–H_2O–CO_2. The $NaAlSi_3O_8$–H_2O–CO_2 system is chosen for the following reasons.

(1) It is a relatively 'simple' system (relatively few components, compared with natural rhyolitic or basaltic compositions).
(2) Abundant experimental and theoretical data exist for this system (e.g. Burnham & Davis, 1971, 1974; Eggler & Kadik, 1979; Bohlen *et al.*, 1982; Hamilton & Oxtoby, 1986; Stolper *et al.*, 1987).
(3) The topology of the $NaAlSi_3O_8$–H_2O–CO_2 system (along with SiO_2–H_2O–CO_2) forms the basis of our current understanding of phase relations in crystallizing melt–volatile systems (Hack *et al.*, 2007).
(4) The *PVTX* thermodynamic relations derived from this system can be extended with confidence to other melt–volatile systems (Burnham & Davis, 1974; Burnham, 1997).
(5) Numerical expressions describing the *PVTX* properties and phase relations in this system are available, or can be developed from existing experimental data.

In the following sections we describe the numerical models used to characterize the *PTX* phase relations on the H_2O-, CO_2- and H_2O–CO_2-saturated albite solidi, the *PTX* dependence of H_2O and CO_2 solubility in the melt phase, and the *PTX* dependence of the molar volumes of melt, vapor and albite.

PTX *correlations on the vapor-saturated solidus*

For the binary systems $NaAlSi_3O_8$–H_2O and $NaAlSi_3O_8$–CO_2, the Gibbs Phase Rule ($f = c - p + 2$) specifies a single degree of freedom if three phases are present, indicating that the system is univariant. Therefore, the three-phase coexistence is described by a line or curve in *PTX* space. We may thus describe *T* as a function of *P* (or vice versa) along the three-phase albite + melt + vapor curve. A consequence of this geometry is that if the temperature of a two-component $NaAlSi_3O_8$–H_2O or $NaAlSi_3O_8$–CO_2 MI containing albite + melt + vapor changes, the internal pressure must change accordingly to maintain all three phases (as discussed in the previous section).

In this study, data for the H_2O-saturated albite solidus from Burnham & Davis (1974) are used. We performed a regression of data for the H_2O-saturated solidus, and used the regression equation to numerically describe *T* on the three-phase curve as a function of *P*. The CO_2-saturated solidus is approximately equal to the dry (H_2O-absent) solidus up to 10 kbar, as shown by Burnham & Davis (1974) and Bohlen *et al.* (1982). We thus represent the CO_2-saturated solidus based on a linear regression of data for the $NaAlSi_3O_8$–H_2O system from Burnham & Davis (1974) where $a_{H_2O} = 0$. The regression equation for the H_2O-saturated solidus is given by

$$T = 888 - 76\ln(P) \quad (6)$$

and that for the CO_2-saturated solidus as

$$T = 1121 + 20P. \quad (7)$$

In both equations, *T* is in degrees Celsius and *P* is in kbar. Equations (6) and (7) reproduce temperature along the solidus curves to within ±1%, over the range 50 bars to 8 kbar for H_2O [equation (6)], and over the range 1 bar to 9 kbar for CO_2 [equation (7)]. The H_2O- and CO_2-saturated solidus curves calculated using equations (6) and (7) are shown in Fig. 4.

For the ternary system $NaAlSi_3O_8$–H_2O–CO_2, the Gibbs' Phase Rule specifies two degrees of freedom if three phases are present, and the system is therefore divariant. Thus, in the ternary system the three-phase coexistence is described by a surface in *PTX* space. In this case, we may describe T as a function of P and X.

In the numerical model, we incorporated the a_{H_2O}-dependent vapor-saturated albite solidus reported by Burnham & Davis (1974, fig. 19) to represent the H_2O–CO_2-saturated solidus and fitted a regression equation to describe T as a function of P and a_{H_2O}. It should be noted that a_{H_2O} refers to the activity of H_2O in both the melt and vapor phases, because we use the same standard state, which is pure H_2O at P and T for both phases. The Burnham & Davis (1974) model was chosen to maintain internal consistency between the *PTX* position of the solidus and the H_2O solubility calculations, which are based on data from Burnham & Davis (1971, 1974). Although significant discrepancy exists between the *PTX* location of the solidus surface from Burnham & Davis compared with the solidus locations reported by Eggler & Kadik (1979) and Bohlen *et al.* (1982), the three models show a similar topology, such that *PTX* trends describing the change in location of the solidus as a function of a_{H_2O} are the same for each of these models. Furthermore, to verify that the *PVTX* evolution predicted in this study is independent of the exact *PTX* coordinates of the solidus surface, reconnaissance modeling using the Bohlen *et al.* (1982) solidus data was conducted and found to yield the same trends as described here based on the Burnham & Davis (1971, 1974) data.

The regression equation describing the *PTX* location of the $NaAlSi_3O_8$–H_2O–CO_2 solidus is given by

$$\begin{aligned} T = \exp(&7\cdot011 - 4\cdot768\times10^{-3}P \\ &+ 4\cdot187\times10^{-4}\tilde{P}^3 + 1\cdot116\times10^{-4}\tilde{P}^4 \\ &- 7\cdot184\times10^{-5}\tilde{P}^5 + 7\cdot414\times10^{-6}\tilde{P}^6 \\ &- 0\cdot3019a_{H_2O} + 2\cdot652\times10^{-2}\tilde{a}^2_{H_2O} \\ &- 0\cdot3884\tilde{a}^3_{H_2O} - 3\cdot394\times10^{-2}\tilde{P}\tilde{a}_{H_2O} \\ &+ 1\cdot895\times10^{-4}\tilde{P}^4\tilde{a}_{H_2O} - 6\cdot057\times10^{-5}\tilde{P}^5\tilde{a}_{H_2O} \\ &+ 5\cdot185\times10^{-6}\tilde{P}^6\tilde{a}_{H_2O}) \end{aligned} \quad (8)$$

where T is in degrees Celsius, P is in kbar, and $\tilde{P} = P - 4{\cdot}255$ and $\tilde{a}_{H_2O} = a_{H_2O} - 0{\cdot}575$. Equation (8) reproduces the Burnham & Davis (1974) albite solidus temperature to within ±3%, over the range 50 bars to 10 kbar and from $a_{H_2O} = 1$ to $a_{H_2O} = 0{\cdot}1$. Equation (8) does not reproduce the most CO_2-rich part of the solidus ($a_{H_2O} < 0{\cdot}1$) because of the pronounced change in the slope and curvature of the solidus that occurs between approximately $a_{H_2O} = 0{\cdot}1$ and $a_{H_2O} = 0$. Iso-activity lines for H_2O calculated from equation (8) are shown in Fig. 4.

Solubilities of H_2O and CO_2 in the melt phase

The solubility of H_2O in the melt phase is described as a function of P, T and the activity of H_2O (a_{H_2O}) by the model of Burnham & Davis [1974, their equations (20) and (21)] and Burnham [1997; his equation (3.6)]. When the volatile component is pure H_2O, the melt is saturated in H_2O when $a_{H_2O} = 1$. When the volatile component is a mixture of H_2O and CO_2, a_{H_2O} is calculated from the equation of state (EOS) for the vapor phase (Holloway, 1977, 1987; Flowers, 1979). Only relatively small differences between $X^{vapor}_{H_2O}$ and a_{H_2O} occur at the *PT* conditions investigated here, which is consistent with the near-ideal mixing of H_2O and CO_2 at these conditions (Holloway, 1977; Flowers, 1979).

The solubility of CO_2 in the melt phase is calculated from the model of Fine & Stolper (1986) as implemented by Holloway & Blank [1994, their equations (13), (22) and (23)] using their parameters for rhyolite melts. Equation (13) of Holloway & Blank is equivalent to equation (4) of Stolper *et al.* (1987), which is specifically for albitic melts. However, here we use the parameters from Holloway & Blank (1994) for rhyolitic melts, rather than the albite melt parameters from Stolper *et al.* (1987), because the model of Stolper *et al.* was fitted to data between 15 and 30 kbar, whereas the parameters of Holloway & Blank (1994) were fitted to data covering a wider range of pressures, including the lower pressure region considered here ($P < 5$ kbar). We note, however, that the *PTX* trends in CO_2 solubility predicted using the parameters from Stolper *et al.* (1987) are identical to those predicted using the parameters from Holloway & Blank (1994).

The CO_2 solubility model requires knowledge of the fugacity of CO_2 (f_{CO_2}) at the given *PTX* conditions. In our implementation, f_{CO_2} is calculated using the EOS for H_2O–CO_2 (Holloway, 1977, 1987; Flowers, 1979).

The solubility of H_2O in the melt is a function of a_{H_2O} whereas the solubility of CO_2 is a function of f_{CO_2}. Thus, as the proportion of CO_2 in the system is increased, a_{H_2O} and H_2O solubility in the melt decrease, whereas f_{CO_2} and CO_2 solubility in the melt increase. Isobars of H_2O and CO_2 solubility in the melt and vapor-phase composition isopleths calculated as described above are shown in Fig. 6. Although there is some difference in absolute values, the magnitudes and trends of the solubility and vapor-phase composition estimates are consistent with values predicted in other studies (Papale, 1999; Newman & Lowenstern, 2002).

Volume of the H_2O, CO_2 and H_2O–CO_2 fluid phase

The EOS of Haar *et al.* (1984) is used to describe the molar volume of pure H_2O as a function of P and T. At magmatic *PT* conditions, H_2O is in the supercritical state and L–V immiscibility is not encountered.

The modified Redlich–Kwong EOS of Holloway (1977, 1987) is used to describe the molar volume of the fluid as a function of P, T and X for pure CO_2 and for H_2O–CO_2 mixtures. The activities and fugacities of the components are also calculated using the EOS (Holloway, 1977, 1987) with the correction reported by Flowers (1979). At magmatic PT conditions, pure CO_2 is always in the supercritical state so L–V immiscibility does not occur, and H_2O and CO_2 are completely miscible at all temperature above 374·1°C, the critical temperature of H_2O (Sterner & Bodnar, 1991). Thus, volatile-phase immiscibility does not occur at magmatic PT conditions for any of the volatile phases considered here. We note, however, that in more complex natural systems containing various salts in addition to H_2O and CO_2, volatile (vapor)-phase immiscibility is common (De Vivo *et al.*, 1995; Frezzotti, 2001).

Volume of the melt phase

The molar volume of the melt phase is calculated from the partial molar volumes of each component in the melt as

$$V^{\text{melt}} = X^{\text{melt}}_{\text{NaAlSi}_3\text{O}_8}\bar{V}^{\text{melt}}_{\text{NaAlSi}_3\text{O}_8} + X^{\text{melt}}_{\text{H}_2\text{O}}\bar{V}^{\text{melt}}_{\text{H}_2\text{O}} + X^{\text{melt}}_{\text{CO}_2}\bar{V}^{\text{melt}}_{\text{CO}_2}. \quad (9)$$

The partial molar volumes of the $NaAlSi_3O_8$ and H_2O components are from Burnham & Davis [1971, their equations (8) and (9)]. The partial molar volume of CO_2 in the melt phase is assigned a constant value of 28·6 $cm^3\,mol^{-1}$ from Lange (1994) after Stolper *et al.* (1987). The variations in partial molar volume of $NaAlSi_3O_8$ and H_2O in the melt along the vapor-saturated solidus at $P \leq 4$ kbar are shown in Fig. 7.

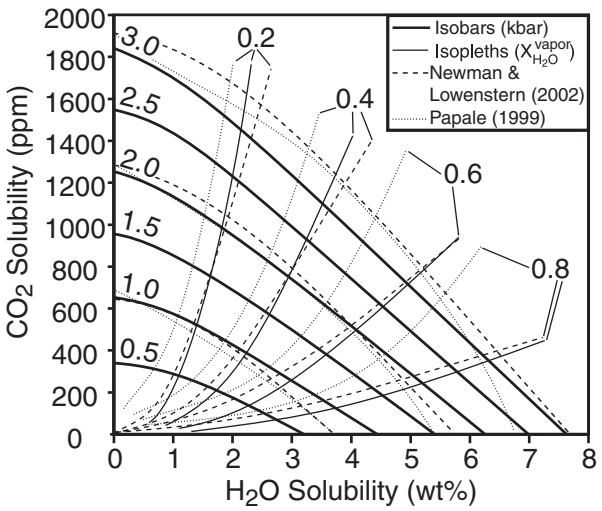

Fig. 6. Isobars (bold continuous lines, labeled in kbars) of H_2O–CO_2 solubility in albite melt at 900°C, based on the data of Burnham & Davis (1974), Fine & Stolper (1986) and Holloway & Blank (1994). Also shown for comparison are solubilities of H_2O–CO_2 in rhyolite melt at 900°C calculated from the models of Newman & Lowenstern (2002; dashed lines) and Papale (1999; dotted lines). Isopleths of the composition of the vapor phase that is in equilibrium with the melt calculated using the three models are also shown and are labeled in mole fraction of H_2O in the vapor.

Volume of the crystallized albite phase

The molar volume of the albite phase is described as a function of P and T by the regression EOS of Burnham & Davis [1971, their equation (6)].

Implementation of the closed, isochoric, post-entrapment crystallization model

Binary $NaAlSi_3O_8$–H_2O and $NaAlSi_3O_8$–CO_2 models

The first step in the numerical model is to define the initial conditions (Fig. 5). A fixed mass of the $NaAlSi_3O_8$ component is selected (because the $PVTX$ evolution path at equilibrium is scale-independent, the actual mass chosen is not important). An initial pressure, or pressure of entrapment of the MI, is specified, and the system is represented by a single-phase vapor-saturated melt. Thus, the initial temperature (the temperature on the vapor-saturated solidus at the initial pressure) is calculated from either equation (6) or (7), depending on which binary system is being considered.

At the initial PT conditions (the trapping conditions), the solubility of H_2O or CO_2 is determined from the solubility model, and that amount of H_2O or CO_2 is added to the melt. The total mass of the MI is the mass of $NaAlSi_3O_8$ plus the mass of the volatile component, either H_2O or CO_2. The molar volume of the melt is calculated from the composition and partial molar volumes of the various components using equation (9) The total MI volume is equal to the initial vapor-saturated melt volume. The total mass and volume of the inclusion (represented by crystals + vapor + melt) remains constant in all subsequent steps as PEC proceeds, to maintain a closed, isochoric system.

PEC is simulated by crystallizing albite from the melt in fixed increments (1% of initial melt mass crystallized at each step). The PEC mass is subtracted from the mass of $NaAlSi_3O_8$ in the melt, and is added to the mass of

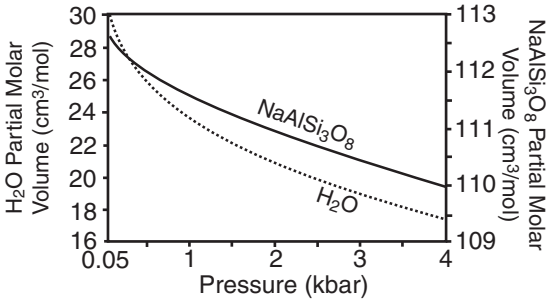

Fig. 7. Variation in partial molar volumes of H_2O (left axis) and $NaAlSi_3O_8$ (right axis) in the melt as a function of pressure along the H_2O-saturated solidus.

crystallized albite (which is initially zero before PEC begins). The mass of H_2O or CO_2 dissolved in the remaining melt is determined from the solubility model, and the remainder (the total mass of H_2O or CO_2 in the MI minus the mass in the melt) is added to the vapor (which is initially zero, before PEC and vapor exsolution begin). The net inclusion volume is calculated as the sum of the volumes of melt plus albite plus vapor.

If the calculated net volume is any value other than the initial volume (± the acceptable tolerance), the pressure is incremented and the temperature, volatile solubility and phase volumes are recalculated. It should be noted that during the pressure iteration, the vapor density and the solubility of H_2O and/or CO_2 in the melt change in response to pressure (and temperature) changes, so these parameters must be recalculated for each pressure iteration. The pressure iteration continues until the net inclusion volume equals the initial volume, and the *PVTX* conditions are recorded, representing the *PVTX* conditions consistent with closed-system, isochoric equilibrium in the MI for the given amount of PEC. The calculation process is repeated as additional increments of albite melt are crystallized.

Ternary $NaAlSi_3O_8$–H_2O–CO_2 system

The calculation method described above for the binary systems applies to the ternary system as well. However, because of the added degree of freedom on the vapor-saturated solidus in the three-component $NaAlSi_3O_8$–H_2O–CO_2 system compared with the binary systems, the iterative procedure used in the ternary model is modified.

To establish the initial conditions, an initial mass of $NaAlSi_3O_8$ is chosen and the initial pressure and temperature in the system are specified. The initial a_{H_2O} is estimated from equation (8) and the solubility of H_2O in the melt phase is calculated as a function of P, T and a_{H_2O}. The composition of the vapor phase that is in equilibrium with a melt having the specified a_{H_2O} is calculated from the EOS of Holloway (1977, 1987) (note that although the vapor composition in equilibrium with the initial melt is calculated, zero grams of vapor are present initially). The solubility of CO_2 in the melt phase is determined as a function of P, T and f_{CO_2} and the masses of H_2O and CO_2 necessary to achieve vapor saturation are added to the melt. The total mass of melt is the sum of the masses of $NaAlSi_3O_8$ plus H_2O plus CO_2. As with the binary models, the total mass, the masses of each of the components and the total volume are held constant in all subsequent steps.

As in the binaries, a fixed mass of albite is crystallized during each step. However, because the solidus in the ternary system is divariant, pressure and a_{H_2O} can vary independently (with T fixed for any P–a_{H_2O} combination). Therefore, to uniquely determine the *PTX* point representing closed-system, isochoric equilibrium for each albite crystallization increment, an additional constraint is required. This constraint is provided by the number of moles of CO_2 in the vapor phase ($n_{CO_2}^{vapor}$), which can be computed by two independent methods, and the values calculated by the two methods are equal at only a single *PTX* point. The iterative procedure therefore involves cycling through values of a_{H_2O} at each pressure increment to find the P–a_{H_2O} combination that satisfies the closed-system isochoric condition as well as the conservation of CO_2 requirement as described below.

First, the mass of H_2O dissolved in the melt phase is determined from the solubility of H_2O at the P and T of interest. The remaining amount of H_2O that cannot be accommodated by the melt is partitioned into the vapor phase. The total mass of H_2O in the vapor phase is converted to moles using the molar mass of H_2O. The mole fraction of CO_2 in the vapor phase is calculated from the a_{H_2O} of the vapor phase using the EOS of Holloway (1977, 1987) for H_2O–CO_2. The number of moles of CO_2 in the vapor is calculated from the number of moles of H_2O in the vapor and the mole fraction of CO_2 in the vapor phase according to

$$n_{CO_2}^{vapor} = \left(\frac{1}{X_{CO_2}^{vapor}} - 1\right)^{-1} n_{H_2O}^{vapor} \quad (10)$$

where $n_{H_2O}^{vapor}$ the number of moles of H_2O in the vapor phase and $X_{CO_2}^{vapor}$ is the mole fraction of CO_2 in the vapor phase.

The number of moles of CO_2 in the vapor phase, $n_{CO_2}^{vapor}$, may also be calculated starting from the melt composition. The number of moles of CO_2 in the melt, $n_{CO_2}^{melt}$, is computed from the solubility of CO_2 in the melt (calculated as a function of P, T and f_{CO_2} using the solubility model) and the number of moles of $NaAlSi_3O_8$ in the melt, according to

$$n_{CO_2}^{melt} = \left(\frac{1}{X_{CO_2}^{melt}} - 1\right)^{-1} n_{NaAlSi_3O_8}^{melt}. \quad (11)$$

The number of moles of CO_2 in the vapor phase equals the number of moles of CO_2 remaining after the amount of CO_2 in the melt phase is subtracted from the total (or bulk) amount of CO_2,

$$n_{CO_2}^{vapor} = n_{CO_2}^{total} - n_{CO_2}^{melt} \quad (12)$$

where $n_{CO_2}^{total}$ is the total number of moles of CO_2 in the MI. The amount of CO_2 in the vapor phase calculated from equations (10) and (12) must be equal to satisfy the requirement of conservation of mass, and this occurs at only a single PT condition.

The iterative procedure employed to determine the closed-system, isochoric, equilibrium *PTX* point corresponding to each increment of albite crystallization is represented by a pair of nested iteration loops, in which a_{H_2O} is

first incremented at constant P to determine the TX point satisfying conservation of CO_2 from equations (10) and (12), followed by P iteration to constrain the PTX condition that satisfies the isochoric conditions that requires constant MI volume. After the $PVTX$ condition that satisfies the closed-system, isochoric equilibrium requirement is determined for a given amount of albite crystallization, the conditions are recorded (output) and the model proceeds to crystallize the next increment of albite. The simulated albite crystallization procedure may be continued to predict the $PVTX$ evolution of the MI to crystallization of 100% of the silicate component if desired.

RESULTS OF SIMULATIONS OF THE *PVTX* EVOLUTION OF MELT INCLUSIONS DURING POST-ENTRAPMENT CRYSTALLIZATION

For each of the $NaAlSi_3O_8$–H_2O, $NaAlSi_3O_8$–CO_2 and $NaAlSi_3O_8$–H_2O–CO_2 systems described above, several PEC simulations were conducted, ranging from 0 to 100% crystallization and starting at various PTX conditions. However, because the amount of PEC reported in studies of natural MI rarely exceeds about 20% (Johnson *et al.*, 2008), we limit the discussion to MI that have experienced ≤25% PEC.

As described in the conceptual model above, the $PVTX$ trend for the $NaAlSi_3O_8$–H_2O system differs significantly from that for $NaAlSi_3O_8$–CO_2, reflecting the significant differences in volumetric properties and solubilities of H_2O and CO_2, as well as differences in the PTX topologies of the $NaAlSi_3O_8$–H_2O and $NaAlSi_3O_8$–CO_2 systems. The ternary system combines features of each of the two end-member systems, and $PVTX$ trends for the ternary system may mimic either of the binaries, depending on the bulk volatile composition of the MI and the amount of PEC.

Below we present examples of the $PVTX$ evolution of MI for the two binary systems and the ternary $NaAlSi_3O_8$–H_2O–CO_2 system. The discussion emphasizes general trends observed in the simulations, which are mainly independent of the specific starting conditions. For each example below, the MI is assumed to be trapped at 2 kbar under vapor-saturated conditions. The PTX evolution trends of the MI up to 25% PEC are summarized in Figures 8–10.

The system $NaAlSi_3O_8$–H_2O

As albite is progressively crystallized from an $NaAlSi_3O_8$–H_2O melt and H_2O vapor is exsolved, the internal pressure in the inclusion increases and the temperature decreases accordingly to maintain PT conditions on the H_2O-saturated solidus (i.e. to maintain the coexistence of three phases, as described above). In the example shown in Fig. 8, an H_2O-saturated MI trapped at 2 kbar shows an increase in internal pressure of ~500 bars (from 2 to ~2·5 kbar) during 25% PEC. This result is consistent with results of Student & Bodnar (1996) for MI in the system H_2O-haplogranite.

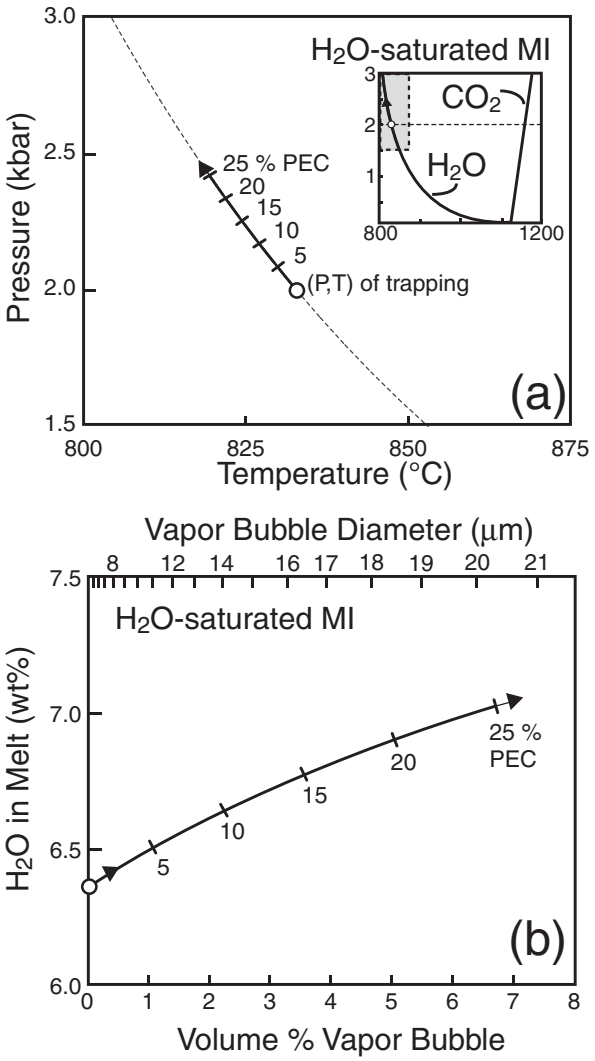

Fig. 8. PTX evolution during PEC of an MI that traps an H_2O-saturated $NaAlSi_3O_8$–H_2O melt at 2 kbar (on the H_2O-saturated solidus). Tick marks on both curves show the mass per cent of albite removed from the melt during PEC, and the arrows on the curves show the PT trend with increasing amount of PEC. (a) Evolution of the temperature and internal pressure of the MI during PEC. Inset shows expanded PT axes, showing the locations of the H_2O-saturated and CO_2-saturated (≈ dry) solidus curves (labeled H_2O and CO_2, respectively), with the shaded box representing the PT area included in the larger diagram. (b) Evolution of H_2O content in the melt (glass) phase as a function of the vapor bubble size. The vapor bubble size is shown as volume per cent of the MI (bottom axis) and vapor bubble diameter (top axis), assuming a spherical vapor bubble and a spherical 50 μm diameter MI.

As H_2O vapor is exsolved from the melt during PEC, the internal pressure increases and this results in an increase in H_2O solubility in the melt phase. Therefore, the melt phase becomes enriched in H_2O (relative to the H_2O content of the melt that was originally trapped in the MI) with increasing crystallization, despite the fact that H_2O is being exsolved from the melt during PEC (Fig. 8). The H_2O content of the melt (glass) phase increases by about 10% during 25% PEC.

The vapor bubble occupies about 6·5 vol. % of the MI after 25% PEC, which corresponds to a spherical bubble with a diameter of about 20 μm in a spherical MI with a diameter of 50 μm (Fig. 8). To calculate the volume per cent occupied by the bubble, we use the expression

$$\text{volume \% bubble} = \frac{\text{volume of vapor}}{\text{volume of vapor} + \text{melt}} \times 100\% \quad (13)$$

which neglects the volume of albite precipitated on the inclusion walls. The albite volume is not included in this calculation because the albite that crystallized during PEC would probably not be recognized during routine petrography—only the melt (glass) phase and the vapor bubble would be recognized. (Note that 25% PEC for a spherical MI that was originally 50 μm in diameter would result in a rim of albite on the walls that is about 2–3 μm thick, and 10% PEC would produce an albite rim ~1 μm thick.) Neglecting the volume of albite that crystallized on the walls during PEC in the computation of the volume per cent bubble means that the volume per cent vapor shown in Figs 8–10 is slightly greater than the volume per cent of vapor that would be estimated if the MI is considered to include melt (glass) + vapor + crystallized albite. It should be noted, however, that the volume of albite crystallized on the walls was included in the iterative calculation to determine the isochoric solution to the PEC model.

The system $NaAlSi_3O_8$–CO_2

In contrast to the MI that traps an H_2O-saturated melt, the internal pressure for a CO_2-saturated MI decreases during PEC. For example, an MI trapped at 2 kbar experiences a pressure decrease of 1500 bars (from 2 to 0·5 kbar) during 25% PEC (Fig. 9). As the pressure decreases during PEC, the temperature also decreases, as is required for the *PTX* conditions to remain on the CO_2-saturated solidus in the $NaAlSi_3O_8$–CO_2 system (Fig. 9).

As the internal pressure in the MI decreases during PEC, the solubility of CO_2 in the melt also decreases, resulting in a lowering of the CO_2 content in the melt phase. In the example shown in Fig. 9, the CO_2 content in the melt phase decreases from about 1350 ppm in the original trapped melt to <400 ppm CO_2 after 25% PEC, representing a decrease of more than 70%. The reduction in CO_2 content in the melt is accompanied by growth of a vapor bubble that occupies about 2 vol. % of the inclusion after 25% PEC. The relatively small volume occupied by the bubble, coupled with the relatively large change in CO_2 content of the melt, illustrates the significant effect that even a small amount of PEC can have on the CO_2 content in the melt. The density of CO_2 in the vapor bubble after 25% PEC is 0·16 g cm^{-3}. According to Rosso & Bodnar (1995), CO_2 vapor with density greater than

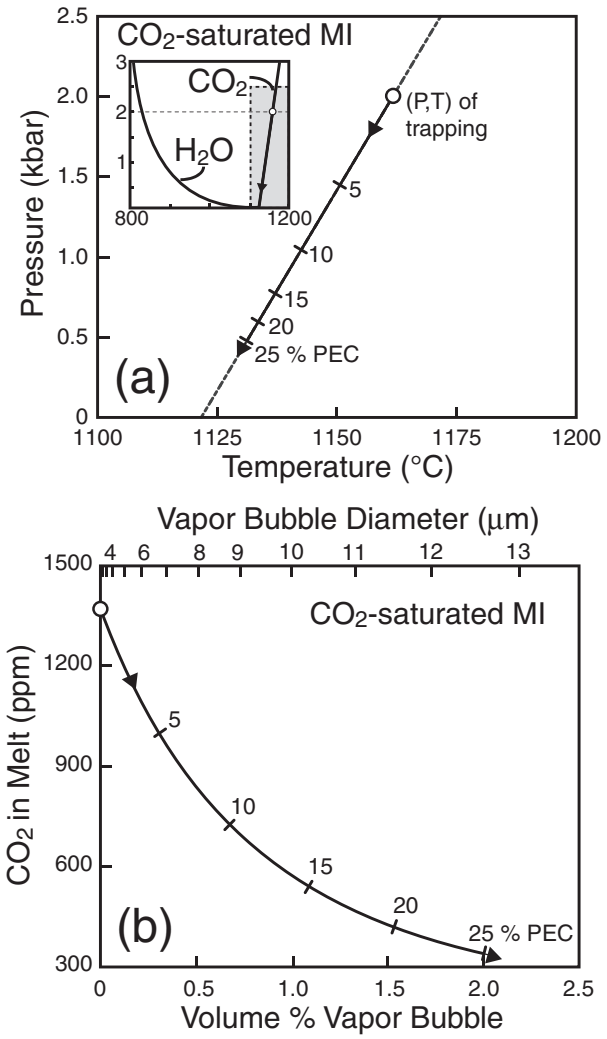

Fig. 9. *PTX* evolution during PEC of an MI that traps a CO_2-saturated $NaAlSi_3O_8$–CO_2 melt at 2 kbar (on the CO_2-saturated solidus). Tick marks on both curves show the mass per cent of albite removed from the melt during PEC, and the arrows on the curves show the *PT* trend with increasing amount of PEC. (a) Evolution of the temperature and internal pressure of the MI during PEC. Inset shows expanded *PT* axes, showing the locations of the H_2O-saturated and CO_2-saturated (≈ dry) solidus curves (labeled H_2O and CO_2, respectively), with the shaded box representing the *PT* area included in the larger diagram. (b) Evolution of CO_2 content in the melt (glass) phase as a function of the vapor bubble size. The vapor bubble size is shown as volume per cent of the MI (bottom axis) and vapor bubble diameter (top axis), assuming a spherical vapor bubble and a spherical 50 μm diameter MI.

about 0·1 g cm^{-3} is readily detectable in inclusions using Raman spectroscopy. Thus the CO_2 in this vapor bubble could be detected by Raman spectroscopic analysis, as was done for the MI in olivine from Procida (Fig. 3) (Esposito *et al.*, 2011).

The system $NaAlSi_3O_8$–H_2O–CO_2

In general, the *PTX* evolution of MI that are saturated in an H_2O–CO_2 vapor phase (Fig. 10) follows a path during the early stage of PEC that is more similar to the CO_2-saturated end-member (see Fig. 9), evolving with continued PEC towards a path that is similar to that of an H_2O-saturated end-member (see Fig. 8). Whereas the mole fraction of H_2O in the melt and that in the vapor in equilibrium with the melt are generally of the same order of magnitude (Fig. 6), the mole fraction of CO_2 in the melt can be several orders of magnitude less than the mole fraction of CO_2 in the vapor because CO_2 partitions preferentially into the vapor phase. Meanwhile, because the activity of H_2O in the system increases with decreasing temperature (Fig. 4), the vapor and melt become increasingly enriched in H_2O as the temperature decreases during continued PEC. The tendency towards increased H_2O in the melt and in the vapor (relative to CO_2) drives the system towards a *PTX* evolution path that is more similar to the path for $NaAlSi_3O_8$–H_2O as PEC continues.

Any H_2O-bearing MI in which a_{H_2O} is less than about 0·95 will follow a *PT* path characterized by an initial decrease in the internal pressure with decreasing temperature during PEC. As the internal pressure decreases, a_{H_2O} increases, and the *PT* evolution undergoes a transition from decreasing pressure to increasing pressure as PEC continues and the *PT* conditions approach the H_2O-saturated solidus. Because the activity of CO_2 in the system is finite (albeit low, at lower temperature), the MI cannot intersect the H_2O-saturated solidus but, rather, approaches it asymptotically (Fig. 10). If crystallization were to continue to >25% PEC (or if the initial trapped melt composition were more H_2O-rich), the internal pressure in the inclusion would continue to increase, and might eventually exceed the trapping pressure (Fig. 10), similar to the trend shown by the H_2O-saturated MI described above (Fig. 8). This dramatic increase in pressure for MI that experience large amounts of PEC provides a likely explanation for the large number of MI in plutonic rocks that appear to have decrepitated during PEC (Student & Bodnar, 2004).

The changes in concentrations of H_2O and CO_2 in an $NaAlSi_3O_8$–H_2O–CO_2 MI during ≤25% PEC are shown in Fig. 10c. The concentration of CO_2 in the original trapped melt is ~520 ppm, and after 25% PEC the CO_2 content of the melt has been reduced to ~60 ppm. Whereas the CO_2 content of the melt phase decreases by an order of magnitude during PEC, the H_2O content increases from ~3·8 to ~4·7 wt %, or about 25% above its initial value. These results are similar to those reported by Blundy & Cashman (2008) for crystallization of a vapor-saturated melt under isobaric conditions. The similarity between the H_2O–CO_2 evolution of melts in a magma body during isobaric crystallization predicted by Blundy & Cashman (2008) and that occurring during isochoric crystallization in an MI reported in this study highlights the importance of careful petrography to identify melt inclusion assemblages (MIA; Bodnar & Student, 2006) and the need to combine volatile data with other geochemical monitors of magma evolution to distinguish between processes that are occurring at the scale of a magma chamber and those that are occurring within single MI.

The reduction in CO_2 content of the melt by an order of magnitude (from ~520 ppm to ~60 ppm) is associated with a vapor bubble that occupies <2·5 vol. % of the MI. As a result, in MI studies the presence of a vapor bubble in the MI should be noted, even if it appears to occupy only a very small proportion of the total MI volume. Also, if possible, the MI should be heated in an attempt to dissolve the volatile phase back into the melt before analysis, and/or the bubbles should be analyzed by Raman spectroscopy to test for the presence of volatiles (especially CO_2) in the bubble. Failure to do so could result in misleading and incorrect interpretations of the MI volatile systematics.

APPLICATION OF MODEL TO OTHER MELT COMPOSITIONS AND HOST PHASES

The quantitative model described here was developed for the system $NaAlSi_3O_8$–H_2O–CO_2 because detailed phase equilibrium and thermodynamic data are available for this system. An important question then is: To what extent do the results presented here apply to melts of other compositions and trapped in host phases other than albite? Data are not available to permit a rigorous quantitative evaluation for all the natural melt compositions and host minerals for MI reported in the literature. However, it is possible to identify some natural melt compositions for which the pressure and volatile evolution paths estimated here for the albite–H_2O–CO_2 system might be applicable.

The volatile evolution path that an MI follows during post-entrapment crystallization is mainly a function of four factors. The first factor, and the one that has the largest effect on the *PT* path, is the absolute solubilities of H_2O and CO_2 in the melt phase. The higher the solubility, the greater the amount of H_2O and/or CO_2 that will be released during crystallization of an aliquot of melt. At 3 kbar and 900°C, the solubility of H_2O in albite melt is 7·6 wt %, compared with a solubility of 7·7 wt % in rhyolite melt at the same conditions, calculated using the VolatileCalc model of Newman & Lowenstern (2002).

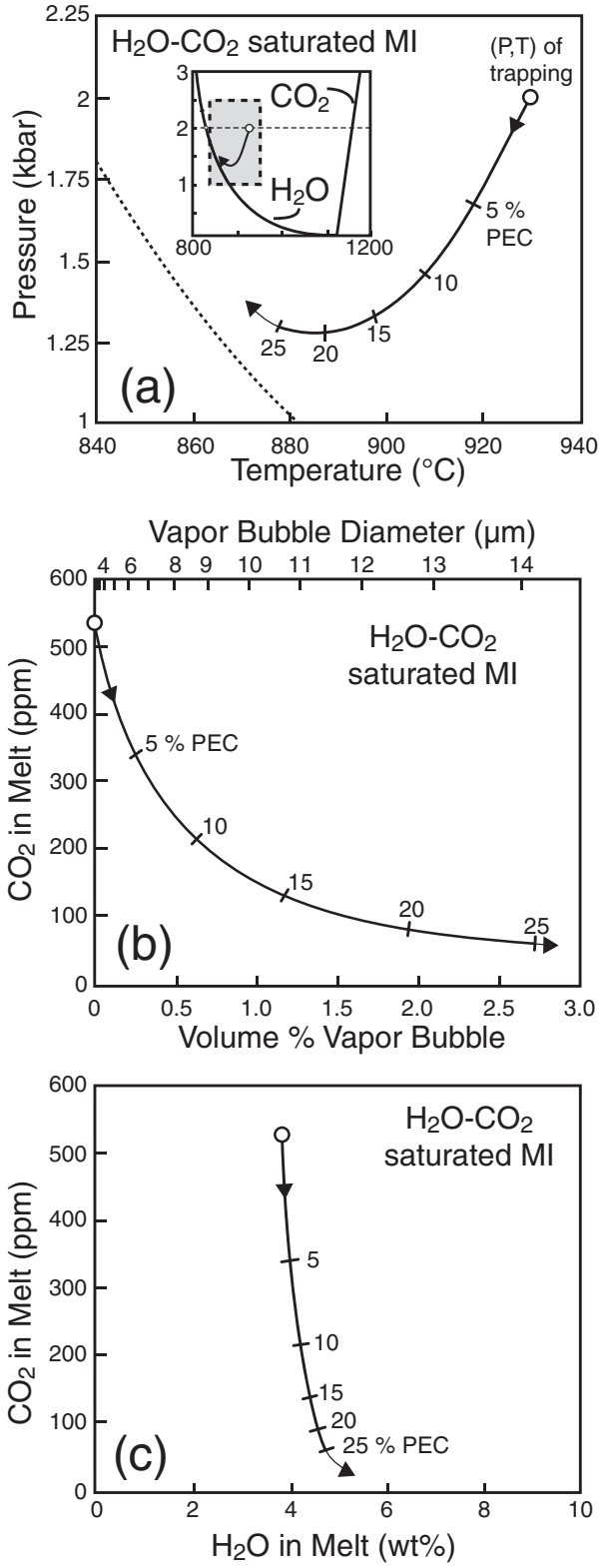

Fig. 10. *PTX* evolution during PEC of an MI that traps a vapor-saturated $NaAlSi_3O_8$–H_2O–CO_2 melt at 2 kbar and 930°C. Tick marks on all graphs show the mass per cent of albite removed from the melt during PEC, and the arrows on the curves show the *PT* trend with increasing amount of PEC. (a) Evolution of the temperature and internal pressure of the MI during PEC. Inset shows expanded *PT* axes, showing the topologies of the H_2O-saturated and CO_2-saturated (≈ dry) solidus curves (labeled H_2O and CO_2, respectively), with the shaded box representing the *PT* area included in the larger diagram. The dashed line shows a portion of the H_2O-saturated solidus. (b) Evolution of CO_2 content in the melt (glass) phase as a function of the vapor bubble size. The vapor bubble size is shown as volume per cent of the MI (bottom axis) and vapor bubble diameter (top axis), assuming a spherical vapor bubble and a spherical 50 μm diameter MI. (c) Evolution in the H_2O–CO_2 concentration of the melt (glass) during PEC and vapor bubble growth.

Moreover, the rate of change in H_2O solubility with changing pressure for albite and rhyolite melts is similar in this *PT* range. As a result, the amount of H_2O that would be exsolved from each increment of rhyolite melt that crystallizes would be essentially the same as the amount exsolved during crystallization of albite melt. Thus, the contribution of H_2O exsolution during PEC to the pressure increase in the MI for a rhyolitic melt would be essentially the same as for albite melts, and we may assume that the results for the albite–H_2O system may be applied to H_2O-rich rhyolitic MI (assuming that the partial molar volume of H_2O in rhyolite melt is similar to its value in albite melt). Moreover, because arc dacites and rhyolites are typically very depleted in CO_2 relative to H_2O (Wallace, 2005, fig. 8), we may further assume that results for the albite–H_2O system are generally applicable to silica-rich (dacitic to rhyolitic) MI.

A second factor that affects the pressure–volatile content path followed by MI during PEC is the relative volume change of the melt phase as the *PT* conditions in the MI change during PEC. This factor (along with the volume of fusion discussed below) constrains the volume available for the exsolved volatiles to occupy, which in turn affects the density of the volatile phase and the pressure in the MI. Because the volume changes associated with thermal expansion are about an order of magnitude larger than those predicted from the compressibility data, we will focus our discussion on the thermal expansion. Few data are available for the thermal expansion and compressibility of real melts, but Lange & Carmichael (1990) summarized the relative volume changes of silicate melts as a function of the oxide components in the melt. The ratios (on a molar basis) of the oxide components Na_2O:Al_2O_3:K_2O:CaO:FeO:Fe_2O_3:MgO in a typical rhyolite melt are 1·0:2·27:0·80:0·35:0·27:0·16:0·17. Using these ratios to approximate the composition of a rhyolite melt and thermal expansion data for these components from Lange & Carmichael (1990, table 3), the average coefficient of thermal expansion for a rhyolite melt is $5{\cdot}30 \times 10^{-3}\,cm^3\,mol^{-1}K^{-1}$, compared with a coefficient of thermal expansion for albite melt (Na_2O) of $7{\cdot}41 \times 10^{-3}\,cm^3\,mol^{-1}K^{-1}$. This means that a rhyolitic melt

will 'shrink' by about 30% less as a result of cooling during PEC. This, in turn, indicates that there will be less volume available to accommodate the exsolved vapor phase, and its density and the internal pressure in the MI will therefore be higher compared with an albite melt. The net result is that the effect on the H_2O content of the melt during PEC will be enhanced relative to the effect predicted for the pure albite MI.

A third factor that affects the pressure–volatile content path followed by the MI during PEC is the volume change of the host phase during cooling. As with the melt phase above, the change in molar volume of the host phase as a result of pressure changes is considerably smaller than that resulting from temperature changes over the limited pressure range investigated here, and we will limit our discussion to the thermal expansion of the host phase. Skinner (1966) summarized thermal expansion data for a wide range of materials, including many common hosts to MI. Over the temperature range 1000°C to 600°C, the molar volume of albite ($Ab_{99}An_1$) decreases by 1·31%. For comparison, over this same temperature range the volume intermediate ($Or_{67}Ab_{33}$) and K-rich ($Or_{83·5}Ab_{16·5}$) alkali feldspar change by 1·43% and 0·96%, respectively. Thus, the change in volume available for the melt to occupy as a result of cooling for MI in intermediate composition feldspars is essentially the same as for MI in albite, whereas the volume change is slightly smaller for K-rich feldspar. For K-rich feldspar hosts, the density of the vapor phase and the internal pressure will be slightly greater compared with MI in albite owing to the smaller volume available for the vapor phase.

The mineral quartz is unlike most other hosts for MI in the sense that the molar volume of β-quartz increases by 0·23% during cooling from 1000°C to 600°C (Skinner, 1966). At temperatures below the quartz α/β transition at ~573°C (at 1 bar pressure), α-quartz shows the more typical behavior of decreasing volume with decreasing temperature. Many MI in volcanic settings are probably trapped in β-quartz (see Student & Bodnar, 1999, fig. 3q). As the MI cools, the volume available for the MI to occupy increases as the molar volume of quartz increases. For all other common mineral hosts for MI, the decrease in volume of the host phase during cooling is to a large extent balanced by the increase in volume available for the bubble owing to shrinkage of the melt during cooling. However, for MI trapped in β-quartz, the volume changes associated with the host phase molar volume change and the change in volume associated with melt phase shrinkage are additive. The net result is that the volume available for the vapor bubble to occupy is larger for MI in quartz, compared with other common host phases, and this in turn will lead to lower densities for the volatile phase in the bubble, and concomitantly lower pressures in the MI and lower volatile solubilities in the remaining melt phase. The effect of the anomalous thermal expansion behavior of quartz on the volatile path was examined by replacing the thermal expansion data for albite with those for β-quartz in our model, leaving all other terms unchanged. The amount of volatiles exsolved and the effect on the path were essentially unchanged from the results for an albite host.

The fourth factor that influences the *PT* volatile path is the volume change associated with crystallization of the melt on the inclusion walls (i.e. the volume of fusion). Lange & Carmichael (1990) summarized volumes of fusion for 12 common minerals, including albite. The volume of fusion of albite is 8·64 $cm^3\,mol^{-1}$. Other reported values are those for sanidine (9·75 $cm^3\,mol^{-1}$), anorthite (5·48 $cm^3\,mol^{-1}$), diopside (12·62 $cm^3\,mol^{-1}$), fayalite (5·49 $cm^3\,mol^{-1}$) and forsterite (5·53 $cm^3\,mol^{-1}$). Bourova & Richet (1998) reported a volume of fusion for β-quartz of 3·85 $cm^3\,mol^{-1}$. Comparing these values, the contribution of crystallization to the volume available for the vapor bubble would be larger for MI in diopside and sanidine (compared with albite-hosted MI), and would be smaller for MI in anorthite and olivine. The result is that the density of the vapor phase and the pressure in MI in diopside and sanidine would be lower compared with MI in albite, and higher in MI in anorthite and olivine. As noted above for the thermal expansion, the volume of fusion for albite was replaced in our model with the volume of fusion of β-quartz, leaving all other parameters unchanged. The result was that during the first few increments of PEC about 60% more CO_2 was exsolved from the melt but that with continued PEC the difference between the albite and β-quartz values decreased. Thus, for small amounts of PEC we could expect slightly greater CO_2 loss from the melt for β-quartz-hosted MI compared with albite-hosted MI, but the differences would disappear for higher amounts of PEC.

Based on the results presented above we conclude that the quantitative model developed for the system albite–H_2O–CO_2 is generally applicable to intermediate composition silicate MI trapped in non-ferromagnesian host minerals. The anomalous thermal expansion of β-quartz suggests that the predicted 'degassing' of the melt in a quartz-hosted MI would be enhanced as the host volume increases while the melt density increases (and its volume decreases). This further suggests that volatile contents of the melt (glass) phase in quartz-hosted MI are even more sensitive to PEC compared with those hosted in albite and other common MI host phases.

DISCUSSION OF MODELING RESULTS—IMPLICATIONS FOR NATURAL MI

The model described here assumes that equilibrium is maintained between the melt, volatile and host phase

during cooling and PEC, while recognizing that such is not always the case for natural MI. It is likely that in nature a rapidly cooled MI may nucleate a vapor bubble without experiencing PEC—in this case the results described here are not applicable.

One of the most striking results of this study is the observation that relatively small amounts of PEC can have a large influence on CO_2 contents of MI that trap CO_2-bearing or H_2O–CO_2-bearing melts. Moreover, a relatively small vapor bubble may contain a significant proportion, if not most, of the CO_2 in the MI. In contrast, the concentration of H_2O in the melt phase is relatively less sensitive to PEC and bubble formation. This result is consistent with the observations of Cervantes *et al.* (2002), who found that CO_2 contents in homogenized MI from picrites from Puu Wahi, Mauna Loa were generally significantly higher (by several hundred ppm) than those in 'naturally quenched', bubble-bearing MI from the same site, whereas the H_2O contents of homogenized and non-homogenized MI showed little difference. Anderson & Brown (1993) corrected for the amount of CO_2 contained in the vapor bubble in natural MI from the 1959 Kilauea Iki picrite by adding to each measured CO_2 content of the melt (glass) an amount of CO_2 that would be contained in a bubble occupying 0·5 vol. % of the inclusion at the vapor pressure of CO_2 in the melt at 1200°C. This correction resulted in an increase in the estimated pressure of trapping by up to a few hundred bars for most MI, and in some cases increased the pressure by more than 1 kbar.

Perhaps the most significant observation of this study is that H_2O–CO_2 trends produced during closed-system PEC and bubble growth in MI (Fig. 10c) are similar to open-system degassing paths. Owing to the lower solubility of CO_2 in the melt compared with H_2O, relatively more CO_2 is lost from the melt phase during ascent and degassing, resulting in a trend in H_2O–CO_2 contents characterized by a wide range in CO_2 contents with relatively small variation in H_2O (Fig. 11a). In Fig. 11a, H_2O–CO_2 data from Lowenstern (1994) are plotted using the same axis scaling as in that study. However, if both axes are scaled to the respective ranges in the data (Fig. 11b), no trend in H_2O vs CO_2 is apparent. In other words, there is no correlation between H_2O and CO_2 contents in this dataset. As such, H_2O–CO_2 data from natural MI rarely show statistically significant trends consistent with open-system degassing paths. Instead, when trends similar to those shown in Fig. 11a are observed, workers often assume that the MI were trapped along a degassing path, with the most CO_2-rich MI being trapped at the greatest depth. Often, no petrographic or other geochemical evidence is offered to support the interpretation that the H_2O–CO_2 trends represent a degassing path.

Open-system degassing is one explanation for the apparent vertical or sub-vertical trends in H_2O–CO_2 contents often observed in studies of MI. The results of this study show that similar H_2O–CO_2 trends may be generated as a result of PEC in vapor-saturated MI. To demonstrate the significance of this point, Fig. 12 shows the H_2O–CO_2 data from Lowenstern (1994), along with an H_2O–CO_2 path that would be produced as a result of PEC, calculated as described above. The calculated trend assumes trapping of an H_2O–CO_2-saturated melt at 4·5 kbar and 895°C, followed by various amounts of PEC. As seen in Fig. 12, the H_2O–CO_2 trend resulting from bubble growth during PEC provides an alternative explanation for the trend in the H_2O–CO_2 data. It should be noted that Lowenstern (1994) analyzed only MI with ≤0·5 vol. % vapor, in an

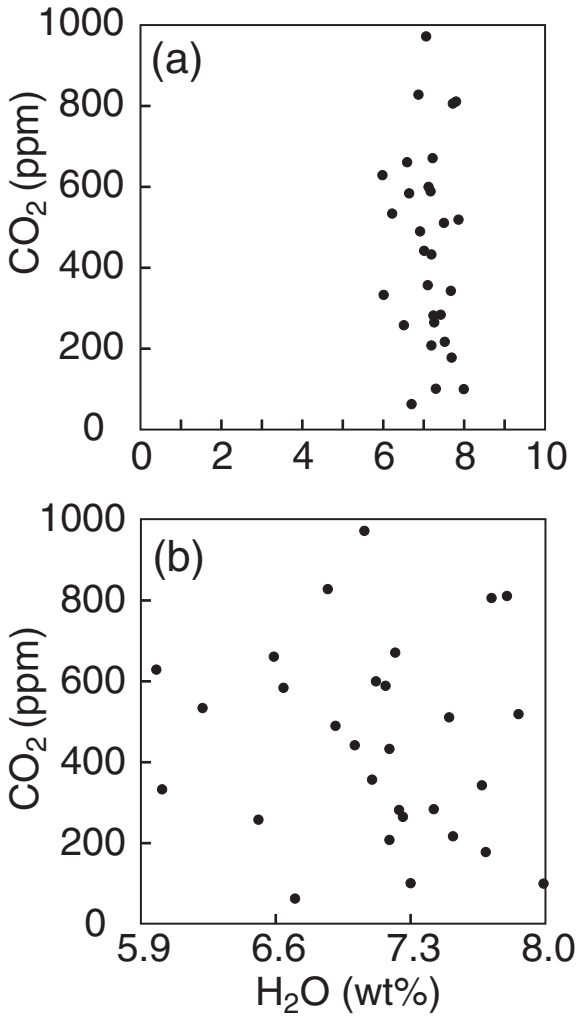

Fig. 11. Concentrations of H_2O–CO_2 in melt inclusions from the Plinian fallout tuff at Pine Grove, Utah, reported by Lowenstern (1994). (a) Pine Grove data with CO_2 axis scaled to the range of the data, and H_2O axis scaled to 5× the range of the data, as originally published by Lowenstern (1994). (b) Same data as plotted in (a), with CO_2 and H_2O axes scaled to the range of the data. When viewed in this manner, it can be seen that there is no statistical correlation between CO_2 and H_2O contents of the MI.

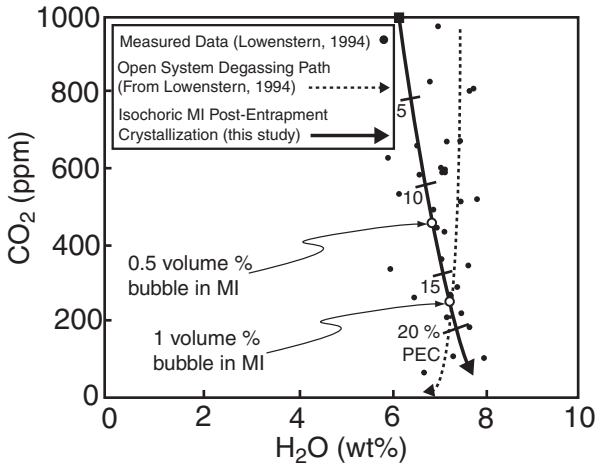

Fig. 12. Comparison of H_2O–CO_2 trends predicted by open-system degassing (dashed line) and as a result of PEC and bubble growth (continuous line). The data points represent the H_2O–CO_2 data of Lowenstern (1994), and the open circles show the points along the PEC path corresponding to 0·5 and 1 vol. % vapor in the MI. Lowenstern (1994) calculated an open-system degassing path for rhyolite using the data and assuming an initial condition of 4·3 kbar and 675°C. The PEC and bubble growth trend was calculated assuming MI trapping at 4·5 kbar and 895°C (the filled square). Either the open-system degassing trend or the PEC trend can be a reasonable interpretation of the data.

effort to eliminate (or minimize) possible errors associated with loss of some of the volatiles to the vapor bubble. However, even if the bubble occupies only 1 vol. % of the MI, the CO_2 content of the melt is reduced by nearly an order of magnitude. Thus, the CO_2 content of the melt can show wide variability as a result of PEC, even if inclusions with only relatively small bubbles are analyzed. We emphasize that we agree with the interpretation of Lowenstern (1994) that the trend shown by MI from Pine Grove is a result of degassing. That is precisely why this is a good example to use for this comparison—the Pine Grove MI define a real degassing path that looks just like a path that would result from PEC, which highlights the difficulty in distinguishing between these phenomena based solely on the H_2O–CO_2 systematics of the MI.

J. B. Lowenstern (personal communication, 2010) noted that the H_2O–CO_2 trends resulting from PEC resemble most closely those for open-system degassing, whereas the model presented here assumes a closed system. The reason for this difference is that calculated closed-system degassing paths are normally isothermal, not isochoric, whereas the PEC calculation in the model is isochoric rather than isothermal. This is an important difference because, in the $NaAlSi_3O_8$–H_2O–CO_2 system, decreasing temperature in the presence of melt + albite + vapor results in an increase in the equilibrium activity of H_2O, and H_2O is thus 'retained' in the melt, and does not exsolve as readily as in the closed-system degassing path. This results in a near-vertical trend in H_2O vs CO_2 concentration, which looks more like a typical open-system degassing path than a typical closed-system degassing path. The important point here is that if an H_2O–CO_2 trend is the result of PEC but is not recognized as such, the trend would probably be interpreted to represent trapping of MI along an open-system degassing path.

Pseudo-degassing paths can also be produced by processes other than PEC. Recently, Gaetani *et al.* (2011) performed re-equilibration experiments to assess the effect of diffusion on H_2O–CO_2 concentrations of glassy MI hosted in olivine. Those workers showed that CO_2 concentrations are unaffected by diffusion, whereas H_2O concentrations are reset on timescales of a few hours. MI with initially different H_2O concentrations, when re-equilibrated with the same magma at the same conditions, attain similar H_2O concentrations. If several MI with a range in volatile concentrations re-equilibrated together, then the MI would consequently have a range of CO_2 concentrations but similar H_2O concentrations. Thus, a suite of MI with a random distribution of H_2O and CO_2 concentrations may develop an apparent H_2O–CO_2 trend resembling an open-system degassing path owing to hydrogen diffusion (Gaetani *et al.*, 2011).

SUMMARY

A rigorous thermodynamic model has been developed to estimate the evolution in volatile contents of melt inclusions during post-entrapment crystallization (PEC) of a vapor-saturated melt under isochoric conditions. Owing to the relatively high solubility of H_2O in silicate melts, combined with the fact that the partial molar volume of H_2O dissolved in the melt is generally much smaller than the molar volume of H_2O in the vapor phase, the internal pressure in an $NaAlSi_3O_8$–H_2O MI increases during PEC and the amount of H_2O in the melt phase increases slightly. Conversely, the internal pressure in an $NaAlSi_3O_8$–CO_2 MI and the CO_2 concentration in the melt phase both decrease during PEC, owing to the lower solubility of CO_2 in the melt and the relatively small difference between the partial molar volume of CO_2 in the melt and the molar volume of CO_2 in the vapor. In MI that trap an $NaAlSi_3O_8$–H_2O–CO_2 melt the internal pressure first decreases during PEC as mostly CO_2 exsolves from the melt, and later increases as the exsolving vapor phase becomes more H_2O-rich. The quantitative model described here is directly applicable to intermediate to silica-rich (dacitic to rhyolitic) MI trapped in host phases that do not contain iron as a major component. For MI trapped in Fe-bearing hosts, trends similar to those described here may be produced through diffusive re-equilibration (Gaetani *et al.*, 2011).

The trends in H_2O–CO_2 contents of MI during PEC and vapor bubble formation are similar to trends expected for open-system degassing of an ascending magma. Without additional supporting data, it may not be possible to determine which process is responsible for producing the observed H_2O–CO_2 trends. Given the potential for PEC and associated bubble formation to affect the volatile concentrations in the melt (glass) phase in MI, we recommend that MI with vapor bubbles be heated to dissolve the volatiles back into the melt, followed by quenching to produce a homogeneous, glassy MI, and/or that the vapor bubbles be analyzed by Raman spectroscopy to test for the presence of CO_2. In addition, the presence or absence of vapor bubbles and the relative bubble size should be recorded and accompany all interpretations of volatile contents of MI.

ACKNOWLEDGEMENTS

The authors thank Leonid Danyushevsky for discussions concerning the use of Petrolog software and implications of post-entrapment crystallization on melt inclusion composition. Discussions with Jim Webster, Luca Fedele and Bob Lowell improved our understanding of the role and behavior of volatiles in melts. Thorough reviews by Jake Lowenstern, Leonid Danyushevsky and Paul Wallace helped to clarify our thinking and significantly improved an earlier version of the paper.

FUNDING

This work was supported by funding from the Institute for Critical Technology and Applied Science at Virginia Tech (M.S.-M.), the US National Science Foundation (R.J.B.) (EAR- 1019770), and Universitá di Napoli Federico II and the Italian Ministry of University Research (R.E.).

REFERENCES

Anderson, A. J. (2010). Accurate phase volume ratio determination of crystal-rich inclusions by focused ion beam milling and microanalysis. *Geochimica et Cosmochimica Acta* **74S**, A19.

Anderson, A. T., Jr & Brown, G. G. (1993). CO_2 contents and formation pressures of some Kilauean melt inclusions. *American Mineralogist* **78**, 794–803.

Anderson, A. T., Davis, A. M. & Lu, F. (2000). Evolution of Bishop Tuff rhyolitic magma based on melt and magnetite inclusions and zoned phenocrysts. *Journal of Petrology* **41**, 449–473.

Blank, J. G., Stolper, E. M. & Carroll, M. R. (1993). Solubilities of carbon dioxide and water in rhyolitic melt at 850°C and 750 bars. *Earth and Planetary Science Letters* **119**, 27–36.

Blundy, J. & Cashman, K. (2008). Petrologic reconstruction of magmatic system variables and processes. In: Putirka, K. D. & Tepley, F. J., III (eds) *Minerals, Inclusions and Volcanic Processes. Mineralogical Society of America and Geochemical Society, Reviews in Mineralogy and Geochemistry* **69**, 179–239.

Bodnar, R. J. & Student, J. J. (2006). Melt inclusions in plutonic rocks: Petrography and microthermometry. In: Webster, J. D. (ed.) *Melt Inclusions in Plutonic Rocks. Mineralogical Association of Canada, Short Course* **36**, 1–26.

Bodnar, R. J., Binns, P. R. & Hall, D. L. (1989). Synthetic fluid inclusions. VI. Quantitative evaluation of the decrepitation behavior of fluid inclusions in quartz at one atmosphere confining pressure. *Journal of Metamorphic Geology* **7**, 229–242.

Bohlen, S. R., Boettcher, A. L. & Wall, V. J. (1982). The system albite–H_2O–CO_2; a model for melting and activities of water at high pressures. *American Mineralogist* **67**, 451–462.

Bourova, E. & Richet, P. (1998). Quartz and cristobalite: High-temperature cell parameters and volumes of fusion. *Geophysical Research Letters* **25**, 2333–2336.

Burnham, C. W. (1979). Magmas and hydrothermal fluids. In: Barnes, H. L. (ed.) *Geochemistry of Hydrothermal Ore Deposits*. New York: John Wiley, pp. 71–136.

Burnham, C. W. (1997). Magmas and hydrothermal fluids. In: Barnes, H. L. (ed.) *Geochemistry of Hydrothermal Ore Deposits*. New York: John Wiley, pp. 63–125.

Burnham, C. W. & Davis, N. F. (1971). The role of H_2O in silicate melts: I. P–V–T relations in the system NaAlSi3O8–H2O to 10 kbar and 1000°C. *American Journal of Science* **270**, 54–79.

Burnham, C. W. & Davis, N. F. (1974). The role of H2O in silicate melts: II. Thermodynamic and phase relations in the system NaAlSi3O8–H2O to 10 kbar, 700° to 1100°C. *American Journal of Science* **274**, 902–940.

Cervantes, P. & Wallace, P. (2003). Magma degassing and basaltic eruption styles; a case study of approximately 2000 year BP Xitle Volcano in central Mexico. *Journal of Volcanology and Geothermal Research* **120**, 249–270.

Cervantes, P., Kamenetsky, V. & Wallace, P. (2002). Melt inclusion volatile contents, pressures of crystallization for Hawaiian picrites, and the problem of shrinkage bubbles. *EOS, Transactions, American Geophysical Union* **83**, F1495–F1496.

Collins, S. J., Pyle, D. M. & Maclennan, J. (2009). Melt inclusions track pre-eruption storage and dehydration of magmas at Etna. *Geology* **37**, 571–574.

Danyushevsky, L. V. (2001). The effect of small amounts of H_2O on crystallisation of mid-ocean ridge and backarc basin magmas. *Journal of Volcanology and Geothermal Research* **110**, 265–280.

Danyushevsky, L. V., Della Pasqua, F. N. & Sokolov, S. (2000). Re-equilibration of melt inclusions trapped by magnesian olivine phenocrysts from subduction-related magmas: petrological implications. *Contributions to Mineralogy and Petrology* **138**, 68–83.

Danyushevsky, L. V., McNeill, A. W. & Sobolev, A. V. (2002). Experimental and petrological studies of melt inclusions in phenocrysts from mantle-derived magmas: an overview of techniques, advantages and complications. *Chemical Geology* **183**, 5–24.

De Vivo, B., Torok, K., Ayuso, R. A., Lima, A. & Lirer, L. (1995). Fluid inclusion evidence for magmatic silicate/saline/CO_2 immiscibility and geochemistry of alkaline xenoliths from Ventotene island, Italy. *Geochimica et Cosmochimica Acta* **59**, 2941–2953.

Eggler, D. H. & Kadik, A. A. (1979). The system $NaAlSi_3O_8$–H_2O–CO_2 to 20 kbar pressure: I. Compositional and thermodynamic relations of liquids and vapors coexisting with albite. *American Mineralogist* **64**, 1036–1048.

Esposito, R., Bodnar, R. J., Danyushevsky, L., De Vivo, B., Fedele, L., Hunter, J., Lima, A. & Shimizu, N. (2011). Volatile evolution of magma associated with the Solchiaro eruption in the Phlegrean Volcanic District (Italy). *Journal of Petrology* **52**, 2431–2460.

Fall, A., Tattitch, B. & Bodnar, R. J. (2011). Combined microthermometric and Raman spectroscopic technique to determine the salinity of H_2O–CO_2–NaCl fluid inclusions based on clathrate melting. *Geochimica et Cosmochimica Acta* **75**, 951–964.

Fedele, L., Bodnar, R. J., DeVivo, B. & Tracy, R. (2003). Melt inclusion geochemistry and computer modeling of trachyte petrogenesis at Ponza, Italy. *Chemical Geology* **194**, 81–104.

Fine, G. & Stolper, E. (1986). Dissolved carbon dioxide in basaltic glasses; concentrations and speciation. *Earth and Planetary Science Letters* **76**, 263–278.

Flowers, G. C. (1979). Correction of Holloway's (1977) adaptation of the modified Redlich–Kwong equation of state for calculation of the fugacities of molecular species in supercritical fluids of geologic interest. *Contributions to Mineralogy and Petrology* **69**, 315–318.

Frezzotti, M.-L. (2001). Silicate-melt inclusions in magmatic rocks; applications to petrology. *Lithos* **55**, 273–299.

Gaetani, G., O'Leary, J. & Shimizu, N. (2011). Post-entrapment changes to H_2O and CO_2 in olivine-hosted melt inclusions. *Mineralogical Magazine* **75**, 879.

Haar, L., Gallagher, J. S. & Kell, G. S. (1984). *NBS/NRC steam tables: thermodynamic and transport properties and computer programs for vapor and liquid states of water in SI units*. Washington, DC: Hemisphere.

Hack, A. C., Thompson, A. B. & Aerts, M. (2007). Phase relations involving hydrous silicate melts, aqueous fluids, and minerals. In: Liebscher, A. & Heinrich, C. A. (eds) *Fluid–Fluid Interactions. Mineralogical Society of America and Geochemical Society, Reviews in Mineralogy and Geochemistry* **65**, 129–185.

Halter, W. E., Pettke, T., Heinrich, C. A. & Rothen-Rutishauser, B. (2002). Major to trace element analysis of melt inclusions by laser-ablation ICP-MS; methods of quantification. *Chemical Geology* **183**, 63–86.

Hamilton, D. L. & Oxtoby, S. (1986). Solubility of water in albite-melt determined by the weight-loss method. *Journal of Geology* **94**, 626–630.

Hauri, E. H. (2002). SIMS analysis of volatiles in silicate glasses 2: Isotopes and abundances in Hawaiian melt inclusions. *Chemical Geology* **183**, 115–141.

Holloway, J. R. (1977). Fugacity and activity of molecular species in supercritical fluids. In: Fraser, D. (ed.) *Thermodynamics in Geology*. Boston, MA: Reidel, pp. 161–181.

Holloway, J. R. (1987). Igneous fluids. In: Carmichael, I. S. E. & Eugster, H. P. (eds) *Thermodynamic Modeling of Geological Materials: Minerals, Fluids and Melts. Mineralogical Society of America, Reviews in Mineralogy* **17**, 211–233.

Holloway, J. R. & Blank, J. G. (1994). Application of experimental results to C–O–H species in natural melts. In: Carroll, M. R. & Holloway, J. R. (eds) *Volatiles in Magmas. Mineralogical Society of America, Reviews in Mineralogy* **30**, 187–230.

Johnson, E. R., Wallace, P. J., Cashman, K. V., Granados, H. D. & Kent, A. J. R. (2008). Magmatic volatile contents and degassing-induced crystallization at Volcan Jorullo, Mexico; implications for melt evolution and the plumbing systems of monogenetic volcanoes. *Earth and Planetary Science Letters* **269**, 477–486.

Kamenetsky, V. S., Pompilio, M., Métrich, N., Sobolev, A. V., Kuzmin, D. V. & Thomas, R. (2007). Arrival of extremely volatile-rich high-Mg magmas changes explosivity of Mount Etna. *Geology* **35**, 255–258.

Kawakami, Y., Yamamoto, J. & Kagi, H. (2003). Micro-Raman densimeter for CO_2 inclusions in mantle-derived minerals. *Applied Spectroscopy* **57**, 1333–1339.

Kent, A. J. R. (2008). Melt inclusions in basaltic and related volcanic rocks. In: Putirka, K. D. & Tepley, F. J., III (eds) *Minerals, Inclusions and Volcanic Processes. Mineralogical Society of America and Geochemical Society, Reviews in Mineralogy and Geochemistry* **69**, 273–331.

Kress, V. C. & Ghiorso, M. S. (2004). Thermodynamic modeling of post-entrapment crystallization in igneous phases. *Journal of Volcanology and Geothermal Research* **137**, 247–260.

Lange, R. A. (1994). The effect of H_2O, CO_2 and F on the density and viscosity of silicate melts. In: Carroll, M. R. & Holloway, J. R. (eds) *Volatiles in Magmas. Mineralogical Society of America, Reviews in Mineralogy* **30**, 331–369.

Lange, R. A. & Carmichael, I. S. E. (1990). Thermodynamic properties of silicate liquids with emphasis on density, thermal expansion and compressibility. In: Nicholls, J. & Russell, J. K. (eds) *Modern Methods of Igneous Petrology: Understanding Magmatic Processes. Mineralogical Society of America, Reviews in Mineralogy* **24**, 25–64.

Lowenstern, J. B. (1994). Dissolved volatile concentrations in an ore-forming magma. *Geology* **22**, 893–896.

Lowenstern, J. B. (1995). Applications of silicate-melt inclusions to the study of magmatic volatiles. In: Thompson, J. F. H. (ed.) *Magmas, Fluids and Ore Deposition. Mineralogical Association of Canada, Short Course* **23**, 71–99.

Lowenstern, J. B. (2003). Melt inclusions come of age; volatiles, volcanoes, and Sorby's legacy. In: De Vivo, B. & Bodnar, R. J. (eds) *Melt Inclusions in Volcanic Systems: Methods, Applications and Problems*. Amsterdam: Elsevier, pp. 1–21.

Lu, F., Anderson, A. T. & Davis, A. M. (1995). Diffusional gradients at the crystal/melt interface and their effect on the composition of melt inclusions. *Journal of Geology* **103**, 591–597.

Mangiacapra, A., Moretti, R., Rutherford, M., Civetta, L., Orsi, G. & Papale, P. (2008). The deep magmatic system of the Campi Flegrei Caldera (Italy). *Geophysical Research Letters* **35**, L21304.

Manley, C. R. (1996). Morphology and maturation of melt inclusions in quartz phenocrysts from the Badlands rhyolite lava flow, southwestern Idaho. *American Mineralogist* **81**, 158–168.

Métrich, N. & Wallace, P. J. (2008). Volatile abundances in basaltic magmas and their degassing paths tracked by melt inclusions. In: Putirka, K. D. & Tepley, F. J., III (eds) *Minerals, Inclusions and Volcanic Processes. Mineralogical Society of America and Geochemical Society, Reviews in Mineralogy and Geochemistry* **69**, 363–402.

Mysen, B. O., Eggler, D. H., Seitz, M. G. & Holloway, J. R. (1976). Carbon dioxide in silicate melts and crystals; Part I, Solubility measurements. *American Journal of Science* **276**, 455–479.

Newman, S. & Lowenstern, J. B. (2002). VolatileCalc; a silicate melt–H_2O–CO_2 solution model written in Visual Basic for Excel. *Computers and Geosciences* **28**, 597–604.

Papale, P. (1999). Modeling of the solubility of a two-component H_2O + CO_2 fluid in silicate liquids. *American Mineralogist* **84**, 477–492.

Papale, P., Moretti, R. & Barbato, D. (2006). The compositional dependence of the saturation surface of H_2O + CO_2 fluids in silicate melts. *Chemical Geology* **229**, 78–95.

Roedder, E. (1979). Origin and significance of magmatic inclusions. *Bulletin de Minéralogie* **102**, 487–510.

Roedder, E. (1984). *Fluid Inclusions. Mineralogical Society of America, Monograph* **12**, , 644 p.

Rosso, K. M. & Bodnar, R. J. (1995). Microthermometric and Raman spectroscopic detection limits of CO_2 in fluid inclusions and the Raman spectroscopic characterization of CO_2. *Geochimica et Cosmochimica Acta* **59**, 3961–3975.

Saito, G., Kazahaya, K., Shinohara, H., Stimac, J. & Kawanabe, Y. (2001). Variation of volatile concentration in a magma system of Satsuma–Iwojima volcano deduced from melt inclusion analysis. *Journal of Volcanology and Geothermal Research* **108**, 11–31.

Schiano, P. (2003). Primitive mantle magmas recorded as silicate melt inclusions in igneous minerals. *Earth-Science Reviews* **63**, 121–144.

Severs, M. J., Azbej, T., Thomas, J. B., Mandeville, C. W. & Bodnar, R. J. (2007). Experimental determination of H_2O loss

from melt inclusions during laboratory heating: Evidence from Raman spectroscopy. *Chemical Geology* **237**, 3–4.

Sisson, T. W. & Layne, G. D. (1993). H_2O in basalt and basaltic andesite glass inclusions from four subduction-related volcanoes. *Earth and Planetary Science Letters* **117**, 619–635.

Skinner, B. F. (1966). Thermal expansion. In: Clark, S. P., Jr (ed.) *Handbook of Physical Constants. Geological Society of America, Memoirs* **97**, 75–96.

Skirius, C. M., Peterson, J. W. & Anderson, A. T., Jr (1990). Homogenizing rhyolitic glass inclusions from the Bishop Tuff. *American Mineralogist* **75**, 1381–1398.

Sobolev, A. V. (1996). Melt inclusions in minerals as a source of principal petrological information. *Petrology* **4**, 209–220.

Spilliaert, N., Allard, P., Métrich, N. & Sobolev, A. V. (2006). Melt inclusion record of the conditions of ascent, degassing, and extrusion of volatile-rich alkali basalt during the powerful 2002 flank eruption of Mount Etna (Italy). *Journal of Geophysical Research* **111**, B40203.

Sterner, S. M. & Bodnar, R. J. (1991). Synthetic fluid inclusions: X. Experimental determination of P–V–T–X properties in the CO2–H2O system to 6 kb and 700°C. *American Journal of Science* **291**, 1–54.

Stolper, E., Fine, G., Johnson, T. & Newman, S. (1987). Solubility of carbon dioxide in albitic melt. *American Mineralogist* **72**, 1071–1085.

Student, J. J. & Bodnar, R. J. (1996). Melt inclusion microthermometry; petrologic constraints from the H_2O-saturated haplogranite system. *Petrology* **4**, 291–306.

Student, J. J. & Bodnar, R. J. (1999). Synthetic fluid inclusions XIV: Coexisting silicate melt and aqueous fluid inclusions in the haplogranite–H_2O–NaCl–KCl system. *Journal of Petrology* **40**, 1509–1525.

Student, J. J. & Bodnar, R. J. (2004). Silicate melt inclusions in porphyry copper deposits; identification and homogenization behavior. *Canadian Mineralogist* **42**, 1583–1599.

Szabo, C., Bodnar, R. J., Sobolev, A. V. & Ayora, C. (1996). Metasomatism associated with subduction-related, volatile-rich silicate melt in the upper mantle beneath the Nograd–Gomor volcanic field, northern Hungary/southern Slovakia: evidence from silicate melt inclusions. *European Journal of Mineralogy* **8**, 881–899.

Thomas, J. B., Bodnar, R. J., Shimizu, N. & Sinha, A. K. (2002). Determination of zircon/melt trace element partition coefficients from SIMS analysis of melt inclusions in zircon. *Geochimica et Cosmochimica Acta* **66**, 2887–2901.

Vigouroux, N., Wallace, P. J. & Kent, A. J. R. (2008). Volatiles in high-K magmas from the western Trans-Mexican volcanic belt; evidence for fluid fluxing and extreme enrichment of the mantle wedge by subduction processes. *Journal of Petrology* **49**, 1589–1618.

Walker, J. A., Roggensack, K., Patino, L. C., Cameron, B. I. & Matias, O. (2003). The water and trace element contents of melt inclusions across an active subduction zone. *Contributions to Mineralogy and Petrology* **146**, 62–77.

Wallace, P. J. (2005). Volatiles in subduction zone magmas: concentrations and fluxes based on melt inclusion and volcanic gas data. *Journal of Volcanology and Geothermal Research* **140**, 217–240.

Webster, J. D. & Duffield, W. A. (1991). Volatiles and lithophile elements in Taylor Creek Rhyolite: constraints from glass inclusion analysis. *American Mineralogist* **76**, 1628–1645.

Zajacz, Z., Hanley, J. J., Heinrich, C. A., Halter, W. E. & Guillong, M. (2009). Diffusive re-equilibration of quartz-hosted silicate melt and fluid inclusions; are all metal concentrations unmodified? *Geochimica et Cosmochimica Acta* **73**, 3013–3027.